NASA/TM—2020-220386

An Improved Plastically Dilatant Unified Viscoplastic Constitutive Formulation for Multiscale Analysis of Polymer Matrix Composites Under High Strain Rate Loading

Christopher Sorini and Aditi Chattopadhyay
Arizona State University, Tempe, Arizona

Robert K. Goldberg
Glenn Research Center, Cleveland, Ohio

January 2020

NASA STI Program . . . in Profile

Since its founding, NASA has been dedicated to the advancement of aeronautics and space science. The NASA Scientific and Technical Information (STI) Program plays a key part in helping NASA maintain this important role.

The NASA STI Program operates under the auspices of the Agency Chief Information Officer. It collects, organizes, provides for archiving, and disseminates NASA's STI. The NASA STI Program provides access to the NASA Technical Report Server—Registered (NTRS Reg) and NASA Technical Report Server—Public (NTRS) thus providing one of the largest collections of aeronautical and space science STI in the world. Results are published in both non-NASA channels and by NASA in the NASA STI Report Series, which includes the following report types:

- TECHNICAL PUBLICATION. Reports of completed research or a major significant phase of research that present the results of NASA programs and include extensive data or theoretical analysis. Includes compilations of significant scientific and technical data and information deemed to be of continuing reference value. NASA counter-part of peer-reviewed formal professional papers, but has less stringent limitations on manuscript length and extent of graphic presentations.

- TECHNICAL MEMORANDUM. Scientific and technical findings that are preliminary or of specialized interest, e.g., "quick-release" reports, working papers, and bibliographies that contain minimal annotation. Does not contain extensive analysis.

- CONTRACTOR REPORT. Scientific and technical findings by NASA-sponsored contractors and grantees.

- CONFERENCE PUBLICATION. Collected papers from scientific and technical conferences, symposia, seminars, or other meetings sponsored or co-sponsored by NASA.

- SPECIAL PUBLICATION. Scientific, technical, or historical information from NASA programs, projects, and missions, often concerned with subjects having substantial public interest.

- TECHNICAL TRANSLATION. English-language translations of foreign scientific and technical material pertinent to NASA's mission.

For more information about the NASA STI program, see the following:

- Access the NASA STI program home page at http://www.sti.nasa.gov

- E-mail your question to help@sti.nasa.gov

- Fax your question to the NASA STI Information Desk at 757-864-6500

- Telephone the NASA STI Information Desk at 757-864-9658

- Write to:
  NASA STI Program
  Mail Stop 148
  NASA Langley Research Center
  Hampton, VA 23681-2199

NASA/TM—2020-220386

An Improved Plastically Dilatant Unified Viscoplastic Constitutive Formulation for Multiscale Analysis of Polymer Matrix Composites Under High Strain Rate Loading

Christopher Sorini and Aditi Chattopadhyay
Arizona State University, Tempe, Arizona

Robert K. Goldberg
Glenn Research Center, Cleveland, Ohio

National Aeronautics and
Space Administration

Glenn Research Center
Cleveland, Ohio 44135

January 2020

Acknowledgments

Christopher Sorini and Aditi Chattopadhyay gratefully acknowledge the support offered by the NASA Harriett G. Jenkins Graduate Fellowship Program Grant #NNX15AU36H.

This work was sponsored by the Advanced Air Vehicle Program
at the NASA Glenn Research Center

Level of Review: This material has been technically reviewed by technical management.

Available from

NASA STI Program
Mail Stop 148
NASA Langley Research Center
Hampton, VA 23681-2199

National Technical Information Service
5285 Port Royal Road
Springfield, VA 22161
703-605-6000

This report is available in electronic form at http://www.sti.nasa.gov/ and http://ntrs.nasa.gov/

An Improved Plastically Dilatant Unified Viscoplastic Constitutive Formulation for Multiscale Analysis of Polymer Matrix Composites Under High Strain Rate Loading

Christopher Sorini and Aditi Chattopadhyay
Arizona State University
Tempe, Arizona 85281

Robert K. Goldberg
National Aeronautics and Space Administration
Glenn Research Center
Cleveland, Ohio 44135

Abstract

Polymer matrix composites are commonly used to fabricate energy-absorbing structures expected to experience impact loading. As such, a detailed understanding of the dynamic response of the constituent materials is necessary. Since the rate, temperature, and pressure dependence of carbon fiber reinforced polymer matrix composites are primarily manifestations of the rate, temperature, and pressure dependence of the polymer matrix, it is crucial that the constitutive behavior of the matrix be accurately characterized. In this work, an existing unified viscoplastic constitutive formulation is extended to ensure thermodynamic consistency and to more accurately account for the tension-compression asymmetry observed in the response of polymeric materials. A new plastic potential function is proposed, and elementary loading conditions are utilized to determine relations between model constants to ensure nonnegative plastic dissipation, a necessary thermodynamic requirement. Expressions for plastic Poisson's ratios are derived and are bounded by enforcing nonnegative plastic dissipation. The model is calibrated against available experimental data from tests conducted over a range of strain rates, temperatures, and loading cases on a representative thermoset epoxy; good correlation between simulations and experimental data is obtained. Temperature rises due to the conversion of plastic work to heat are computed via the adiabatic heat energy equation. The viscoplastic polymer model is then used as a constitutive model in the generalized method of cells micromechanics theory to investigate the effects of matrix adiabatic heating on the high strain rate response of a unidirectional composite. The thermodynamic consistency of the model ensures plastic dissipation can only cause an increase in temperature. Simulation results indicate that significant thermal softening due to the conversion of plastic work to heat is observed in the composite for matrix dominated deformation modes.

1.0 Introduction

Due to their excellent energy absorption capability, carbon fiber reinforced polymer matrix composites (PMCs) are often used in aerospace applications such as jet engine fan blade containment systems that are subjected to high velocity impact loading in the event of blade-out. The energy is absorbed through various complicated deformation and damage mechanisms, some of which are difficult to detect experimentally. A thorough understanding of the material response under dynamic conditions is therefore required for the assurance of structural reliability and safety of composites in such mission critical components. To this end, physics based constitutive models that span the relevant length scales and capture key deformation, damage, and failure mechanisms in an impact event are indispensable tools that could expedite the design and certification timeline of impact resistant PMC structures.

The development of predictive computational models for PMCs under impact loading conditions is complicated by the inherent material heterogeneity and anisotropy, the multiscale nature (i.e., disparity of length scales associated with constituent materials, tows, braid/weave architecture, and structural components), and complex interactions between the fiber reinforcement and the strain rate, temperature, and pressure dependent polymer matrix. Unlike metals, for which inelastic deformation is generally considered to be deviatoric (volume preserving and pressure independent), the inelastic deformation of polymers, and therefore of PMCs, is known to be pressure dependent (Kolling et al. 2005, Siviour and Jordan 2016). Additionally, high rate deformation is not isothermal, as is often erroneously assumed. It is well known that a portion of the work required to inelastically deform polymeric materials is dissipated as heat (Chou et al. 1973, Arruda et al. 1995, Rittell 1999, Garg et al. 2008), particularly at high strain rates. Under quasi-static conditions, where the duration of loading is large compared to the characteristic thermal diffusion time, heat generated locally due to plastic dissipation has sufficient time to diffuse throughout (and convect away from) the deforming body, which remains in an isothermal condition. As the rate of deformation increases, the rate of heat generation gradually exceeds the rate of heat loss due to conduction/convection, resulting in a gradual temperature rise in the material. Under high rate deformation, where the duration of loading is negligible compared to the characteristic thermal diffusion time, there is insufficient time for significant heat transfer to occur and adiabatic conditions prevail. Adiabatic conditions can therefore be assumed for dynamic loading (Li and Lambros 2001, Kendall and Siviour 2013, Trojanowski 1997, Garg et al. 2008, Chou et al. 1973). Local adiabatic temperature rises, which could exceed the matrix glass transition temperature (Johnston et al. 2018), cause thermal softening (Arruda, et al. 1995, Garg et al. 2008, Rittell 1999) and a potentially substantial effect on the high rate constitutive behavior of polymers and PMCs if the effects of thermal (and intrinsic) softening outweigh the effects of strain and strain rate hardening (Li and Lambros 2001, Chiou et al. 2007, Walley et al. 1989).

Metal plasticity theory has often been used to model the nonlinear deformation of PMCs, despite the well-known pressure dependence of the plastic deformation of polymers. A manifestation of this pressure dependence is tension-compression asymmetry; the magnitude of the compressive yield stress is greater than the tensile yield stress (Kolling et al. 2005, Siviour and Jordan 2016). However, metal plasticity theories suffer from two primary disadvantages when applied to pressure sensitive materials. These theories assume plastic deformation is i) independent of hydrostatic stress and ii) plastic deformation is deviatoric (volume preserving). As such, inelastic constitutive laws based on the isotropic von Mises or anisotropic Hill yield criteria are generally not suitable for pressure sensitive materials, such as polymers, soils, and composites with pressure sensitive matrices.

The development of macroscopic pressure-dependent plasticity models for composites has been investigated by many authors (Kenaga et al. 1987, Sun and Chen 1989, Chen and Sun 1993, Robinson et al. 1994, Chen et al. 1997, Thiruppukuzhi and Sun 1998, Weeks and Sun 1998, Robinson and Binienda 2001, Yokozeki et al. 2007, Wang and Xiao 2017a, Wang and Xiao 2017b). Kenaga et al. (1987) proposed a pressure-dependent quadratic plastic potential function and used an associated flow rule to derive a three-parameter plane stress elastic-plastic model to simulate the quasi-static nonlinear behavior of a boron/aluminum composite. Sun and Chen (1989) extended the model of Kenaga et al. (1987) by noting that most unidirectional composites exhibit an essentially linear elastic response in the fiber direction; enforcing this condition resulted in a one-parameter elastic-plastic model. It should be noted that Sun and Chen's (1989) one-parameter potential can be deduced from Hill's pressure-independent plastic potential by assuming no plasticity in the fiber direction and a state of plane stress (Chen and Sun 1993, Chen et al. 1997), which implies the model's pressure dependence is due to said assumptions. The aforementioned macroscopic plasticity models are limited to quasi-static plane stress conditions.

To model the high strain rate behavior of PMCs, Thiruppukuzhi and Sun (1998) used a three-dimensional (3D) pressure-dependent quadratic plastic potential to develop a power law viscoplasticity model. Assumptions of transverse isotropy and no plasticity in the fiber direction result in a one-parameter plastic potential. However, said assumptions result in a pressure-independent potential. Weeks and Sun (1998) used the 3D plastic potential proposed by Chen and Sun (1993) to develop two 3D rate-dependent plasticity models. The authors assume no plasticity in the fiber direction and transverse isotropy, which reduces the potential to that used by Thiruppukuzhi and Sun (1998). Robinson et al. (1994) and Robinson and Binienda (2001) extended the isotropic unified viscoplastic Bodner-Partom (Bodner and Partom 1975) model to account for transverse isotropy and hydrostatic stress dependence by proposing an effective stress that depends on pressure and other invariants that reflect transverse isotropy. Bounds on material constants were determined by considering natural stress states for the model. It should be noted that none of the aforementioned macroscopic plasticity models are able to account for tension-compression asymmetry since they are all based on plastic potential functions that are *even* functions of hydrostatic stress.

Yokozeki et al. (2007) proposed a simple extension to the one-parameter Sun and Chen (1989) model to incorporate tension-compression asymmetry. This was done by adding a hydrostatic pressure term (and associated model constant) to the effective stress given by Sun and Chen (1989). An extra term was also added into the square root term in the effective stress to ensure the plastic potential is nonnegative. The value of the hydrostatic constant to guarantee a nonnegative effective stress was not mentioned, though it is trivial to determine that the value should be less than or equal to $\sqrt{2}/2$ for the plane stress case. Starting with a generalized anisotropic yield function, Wang and Xiao (2017a) took a similar approach to Yokozeki et al. (2007) and extended the one-parameter Sun and Chen (1989) model to capture tension-compression asymmetry. The model, which incorporates a parameter that represents the ratio of transverse tensile to compressive yield stress, is rate dependent and is applicable to plane stress conditions. The model was later extended by the authors to be fully three-dimensional (Wang and Xiao 2017b).

The aforementioned plasticity formulations are macroscopic in that they treat the composite as a smeared homogeneous continuum. The macromechanical approach is advantageous in that it is computationally efficient and the experimental testing used for model calibration implicitly accounts for all in-situ effects (interface, damage, residual stresses, etc.) (Aboudi et al. 2012). Despite the advantages of macromechanical models, their calibration requires extensive experimental testing (each variation in fiber volume fraction, architecture, orientation, and constituent material properties must essentially be characterized like a new material) and requires the application of more advanced constitutive and damage/failure theories (i.e., anisotropic). Moreover, the macromechanical approach only tends to work well for fiber dominated loading scenarios and in the linear, isothermal deformation regime (Aboudi et al. 2012). In micromechanical approaches, the individual constituents are explicitly modeled; constituent interaction is realized through homogenization, which allows prediction of the effective composite behavior based on the properties, arrangement, and volume fractions of the constituents (Aboudi et al. 2012). The micromechanical approach, though more computationally expensive, is advantageous in that it is highly accurate, able to resolve constituent fields, and allows the application of simpler constitutive and damage/failure models at a more fundamental length scale (constituent level) than the macromechanical approach.

The isotropic von Mises yield criterion has been used to model the polymer matrix constituent in micromechanics-based multiscale models of PMCs and metal matrix composites (MMCs). The unified Bodner-Partom viscoplasticity model (Bodner and Partom 1975, Bodner 2001) has been widely used due to its simplicity and accuracy and can easily be incorporated into multiscale micromechanical approaches. The model has a single isotropic state variable to simulate isotropic hardening and uses an effective stress based on the J_2 flow potential and is, therefore, pressure independent. Bednarcyk et al. (2019) developed a higher-order two-way thermochemically coupled multiscale micromechanics model to investigate the impact response of carbon/epoxy and SiC/Ti composites, where the Bodner-Partom (Bodner and Partom 1975) viscoplastic model was employed to model the viscoplastic response of the epoxy and Ti matrices, respectively. The Bodner-Partom (Bodner and Partom 1975) model was extended by Goldberg et al. (2005) to include hydrostatic stress effects. This was accomplished by modifying the Bodner-Partom (Bodner and Partom 1975) plastic potential to also depend on hydrostatic stress. In addition to an isotropic hardening state variable, the Goldberg model (Goldberg et al. 2005) employs a single scalar state variable, α, to account for the level of influence of hydrostatic stress on plastic deformation.

In previous work by the authors (Sorini et al. 2019), the Goldberg model (Goldberg et al. 2005) was extended to nonisothermal conditions and was used as a constitutive model in the generalized method of cells (GMC) (Aboudi et al. 2012, Paley and Aboudi 1992, Pindera and Bednarcyk 1999) micromechanics framework to investigate the effects of matrix adiabatic heating and thermal softening on the high rate deformation of a unidirectional T700/Epon 862 (T700/E862) composite. The model (Sorini et al. 2019) is strain rate, temperature, and pressure dependent, captures tension-compression asymmetry, and lends itself well to incorporation into commercial finite element codes and micromechanics-based multiscale schemes. However, despite the ability of the Goldberg model (Goldberg et al. 2005) and the nonisothermal extension (Sorini et al. 2019) to capture tension-compression asymmetry, there is no way to independently control the magnitudes of the tensile and compressive saturation stresses (the stresses where the stress-strain curve flattens out) due to the single hydrostatic state variable. A consequence of this is that once the models (Goldberg et al. 2005, Sorini et al. 2019) are calibrated based on experimental shear and uniaxial tensile stress-strain data, for example, there is no way to characterize the models to match uniaxial compressive stress-strain data. The hydrostatic state variable can be related to the plastic Poisson's ratio, which is defined analogously to the elastic Poisson's ratio and is described in more detail later in the manuscript. However, values of the hydrostatic state variable that correspond to physically realistic values of the tensile plastic Poisson's ratio correspond to physically unrealistic values of the compressive plastic Poisson's ratio and vice-versa. Lastly, certain loading conditions can result in negative plastic dissipation. This is problematic because, according to the second law of thermodynamics, plastic dissipation must be nonnegative in the absence of damage and heat conduction (Chow and Lu 1989, Faria et al. 1998, Kawai et al. 2010). Negative plastic dissipation implies a decrease in temperature due to inelastic deformation, which is nonphysical. Even though a negative plastic work density was not observed in the simulated loading conditions considered in the previous work (Sorini et al. 2019), it is essential to prevent this possibility to ensure thermodynamic consistency of the model for general multiaxial loading.

In this work, several improvements are made to the Goldberg model (Goldberg et al. 2005). The model is extended to i) more accurately account for the tension-compression asymmetry observed in the response of polymeric materials; ii) ensure physically realistic plastic flow; iii) ensure thermodynamic consistency (i.e., nonnegative plastic dissipation). A new plastic potential function is proposed, where two constants control the level of influence of hydrostatic stresses on the inelastic deformation. Elementary loading conditions are utilized to determine relations between the hydrostatic constants to ensure nonnegative plastic dissipation. Expressions for plastic Poisson's ratios are derived and are bounded by

enforcing nonnegative plastic dissipation. The proposed plastic potential function allows the user to independently specify the tensile and compressive plastic Poisson's ratios and is capable of simulating nonisochoric plastic deformation. The constitutive model is calibrated against available Epon 862 (E862) epoxy resin shear, tensile, and compressive data (Gilat et al. 2007, Littell 2008, Littell et al. 2008) from tests conducted over a range of strain rates and temperatures. Temperature rises due to the conversion of plastic work to heat are computed via the adiabatic heat energy equation; the thermodynamic consistency of the model ensures plastic dissipation can only lead to an increase in temperature. The unified viscoplastic model is then used as a constitutive model in the generalized method of cells (GMC) (Aboudi et al. 2012, Paley and Aboudi 1992, Pindera and Bednarcyk 1999) micromechanics framework to illustrate the effects of adiabatic heating on the response of a T700/E862 unidirectional composite. A micromechanics-based multiscale approach is used to allow adiabatic heating to be modeled at the matrix constituent level, where it has been experimentally observed to be predominant (Johnston et al. 2018) in flat panel impact tests on triaxially braided PMC panels. Significant thermal softening due to adiabatic heating is observed for matrix dominated deformation modes (transverse tension, transverse compression, and in-plane shear), highlighting the importance of including the effects of adiabatic heating in multiscale analyses of PMCs under dynamic loading, where the composite is in a complex multiaxial stress state. The intended application of the improved unified viscoplastic constitutive formulation is the multiscale analysis of PMCs subjected to impact loading, where it is suitable to predict the rate, temperature, and pressure dependent inelastic deformation, as well as adiabatic heating and subsequent thermal softening, of the polymer matrix.

2.0 Plastically Dilatant Unified Viscoplastic Constitutive Model

As in previous work by the authors (Sorini et al. 2019, Goldberg et al. 2005), unified viscoplasticity theory is utilized. Unlike classical plasticity models, unified viscoplasticity models do not employ a defined yield surface or load-unload conditions. Rather, nonlinearity is controlled by the evolution of state variables that represent the average effects of various deformation mechanisms. The term "unified" implies that no distinction is made between rate-dependent viscoplastic and rate-independent plastic strains (Lubliner 2008). Instead, a single (i.e., unified) inelastic strain tensor is present for all levels of stress, where the components are nominal in the "elastic" deformation regime. The fact that inelastic strains are always present is a consequence of the lack of a yield surface.

Since the constitutive behavior of polymeric materials is pressure dependent, a piecewise plastic potential function that is a function of the first invariant of the Cauchy stress tensor, σ_{kk}, and the second invariant of the deviatoric stress tensor, J_2, is defined as:

$$f = \begin{cases} \sqrt{J_2} + A\sigma_{kk} & \text{if } \sigma_{kk} \neq 0 \text{ and } J_2 \neq 0 \\ \sqrt{J_2} & \text{if } \sigma_{kk} = 0 \text{ and } J_2 \neq 0 \\ A\sigma_{kk} & \text{if } \sigma_{kk} \neq 0 \text{ and } J_2 = 0 \end{cases} \tag{1}$$

In Equation (1), $A = \left(\sqrt{\gamma}\,\text{sign}\left(\sigma_{kk}\right) + \xi\right)$ and γ and ξ are constants that control the influence of hydrostatic stress on plastic deformation. The hydrostatic constant γ must be nonnegative whereas the implications of positive, negative, and zero valued ξ is discussed later in the manuscript. An associative flow rule is used, where the components of the inelastic strain rate tensor, $\dot{\varepsilon}_{ij}^{I}$, are assumed to be equal to

the product of the partial derivative of the plastic potential function, f, with respect to the components of the Cauchy stress tensor, σ_{ij}, and the scalar rate of the plastic multiplier, $\dot{\lambda}$, as follows:

$$\dot{\varepsilon}_{ij}^{I} = \dot{\lambda}\frac{\partial f}{\partial \sigma_{ij}} \tag{2}$$

Taking the partial derivative of the plastic potential function with respect to the components of the Cauchy stress tensor results in the following:

$$\frac{\partial f}{\partial \sigma_{ij}} = \begin{cases} \dfrac{s_{ij}}{2\sqrt{J_2}} + A\delta_{ij} & \text{if } \sigma_{kk} \neq 0 \text{ and } J_2 \neq 0 \\ \dfrac{s_{ij}}{2\sqrt{J_2}} & \text{if } \sigma_{kk} = 0 \text{ and } J_2 \neq 0 \\ A\delta_{ij} & \text{if } \sigma_{kk} \neq 0 \text{ and } J_2 = 0 \end{cases} \tag{3}$$

In Equation (3), s_{ij} are the components of the deviatoric stress tensor and δ_{ij} is the Kronecker delta. The reason for employing a piecewise plastic potential function is because the partial derivative of $\sqrt{J_2} + A\sigma_{kk}$ with respect to σ_{ij} is not defined for pure shear, $\sigma_{kk} = 0$ and $J_2 \neq 0$, (derivative of sign function is not defined when its argument is zero: $\frac{\partial A}{\partial_{\sigma_{ij}}} = \frac{\partial}{\partial_{\sigma_{ij}}}\left(\sqrt{\gamma}\,\text{sign}\left(\sigma_{kk}\right) + \xi\right) = 0$ when $\sigma_{kk} \neq 0$) or purely hydrostatic loading, $\sigma_{kk} \neq 0$ and $J_2 = 0$ (division by $J_2 = 0$). The piecewise definition of the plastic potential also prevents plastic dilation under pure shear loading. The rate of the plastic multiplier, $\dot{\lambda}$, is obtained by substituting Equation (3) into Equation (2) and taking the tensor product of the inelastic strain rate tensor with itself. The result is shown in Equation (4).

$$\dot{\lambda} = \begin{cases} \sqrt{\dfrac{2\dot{\varepsilon}_{ij}^{I}\dot{\varepsilon}_{ij}^{I}}{1+6A^2}} & \text{if } \sigma_{kk} \neq 0 \text{ and } J_2 \neq 0 \\ \sqrt{2\dot{\varepsilon}_{ij}^{I}\dot{\varepsilon}_{ij}^{I}} & \text{if } \sigma_{kk} = 0 \text{ and } J_2 \neq 0 \\ \sqrt{\dfrac{\dot{\varepsilon}_{ij}^{I}\dot{\varepsilon}_{ij}^{I}}{3A^2}} & \text{if } \sigma_{kk} \neq 0 \text{ and } J_2 = 0 \end{cases} \tag{4}$$

Next, the effective stress is defined as

$$\sigma_e = \sqrt{3}f = \begin{cases} \sqrt{3J_2} + \sqrt{3}A\sigma_{kk} & \text{if } \sigma_{kk} \neq 0 \text{ and } J_2 \neq 0 \\ \sqrt{3J_2} & \text{if } \sigma_{kk} = 0 \text{ and } J_2 \neq 0 \\ \sqrt{3}A\sigma_{kk} & \text{if } \sigma_{kk} \neq 0 \text{ and } J_2 = 0 \end{cases} \tag{5}$$

It is evident from Equation (5) that, under pure shear loading, or if the hydrostatic constants γ and ξ are both equal to zero, the effective stress simplifies to the classical definition of $\sqrt{3J_2}$, which reduces to the

applied stress for uniaxial tensile and compressive loading. The effective inelastic strain rate, $\dot{\varepsilon}_e^I$, is determined by invoking the principle of the equivalence of plastic work rate density:

$$\dot{W}^I = \sigma_{ij}\dot{\varepsilon}_{ij}^I = \sigma_e\dot{\varepsilon}_e^I \geq 0 \tag{6}$$

By combining Equations (2) and (3), substituting the result as well as the effective stress (Eq. (5)) into Equation (6), the effective inelastic strain rate is determined and shown in Equation (7).

$$\dot{\varepsilon}_e^I = \begin{cases} \sqrt{\dfrac{2\dot{\varepsilon}_{ij}^I\dot{\varepsilon}_{ij}^I}{3\left(1+6A^2\right)}} & \text{if } \sigma_{kk} \neq 0 \text{ and } J_2 \neq 0 \\ \sqrt{\dfrac{2}{3}\dot{\varepsilon}_{ij}^I\dot{\varepsilon}_{ij}^I} & \text{if } \sigma_{kk} = 0 \text{ and } J_2 \neq 0 \\ \dfrac{\sqrt{\dot{\varepsilon}_{ij}^I\dot{\varepsilon}_{ij}^I}}{3|A|} & \text{if } \sigma_{kk} \neq 0 \text{ and } J_2 = 0 \end{cases} \tag{7}$$

By inspecting Equation (4) and Equation (7), it is apparent that $\dot{\lambda} = \sqrt{3}\dot{\varepsilon}_e^I$. Note that if the hydrostatic constants are set to zero, $A = 0$; in this case, $\dot{\varepsilon}_e^I$ should be set to zero for the $\sigma_{kk} \neq 0$ and $J_2 = 0$ case in a numerical code to avoid division by zero. By defining

$$\frac{\sqrt{3}}{2}\dot{\varepsilon}_e^I = \frac{\dot{\lambda}}{2} = D_0 \exp\left[-\frac{1}{2}\left(\frac{Z}{\sigma_e}\right)^{2n}\right] \tag{8}$$

based on the work of Bodner and Partom (1975) and Bodner (2001), and combining Equation (2), Equation (3) and Equation (8), the inelastic strain rate tensor components are obtained.

$$\dot{\varepsilon}_{ij}^I = \begin{cases} 2D_0 \exp\left[-\dfrac{1}{2}\left(\dfrac{Z}{\sigma_e}\right)^{2n}\right]\left(\dfrac{s_{ij}}{2\sqrt{J_2}} + A\delta_{ij}\right) & \text{if } \sigma_{kk} \neq 0 \text{ and } J_2 \neq 0 \\ 2D_0 \exp\left[-\dfrac{1}{2}\left(\dfrac{Z}{\sigma_e}\right)^{2n}\right]\left(\dfrac{s_{ij}}{2\sqrt{J_2}}\right) & \text{if } \sigma_{kk} = 0 \text{ and } J_2 \neq 0 \\ 2D_0 \exp\left[-\dfrac{1}{2}\left(\dfrac{Z}{\sigma_e}\right)^{2n}\right]\left(A\delta_{ij}\right) & \text{if } \sigma_{kk} \neq 0 \text{ and } J_2 = 0 \end{cases} \tag{9}$$

In Equations (8) and (9), n is a constant that controls strain rate sensitivity (as n increases, rate dependence decreases), D_0 is a constant scale factor that represents the maximum inelastic strain rate, and Z is a scalar state variable that represents the resistance to internal stress (captures isotropic hardening). The state variable Z evolves from its initial value of Z_0 to its final value of Z_1, where $Z_1 > Z_0$, according to the following expression:

$$\dot{Z} = q\left(Z_1 - Z\right)\dot{\varepsilon}_e^I \tag{10}$$

where q is a constant that controls the hardening rate. It should be noted that an effective stress of zero implies no inelastic deformation; to prevent division by zero in a numerical code, the components of the inelastic strain rate tensor (Eq. (9)) should be set to zero in this case.

2.1 Temperature Dependent Plastic Flow

To account for the temperature dependence of the saturation stress, the components of the inelastic strain rate tensor are modified to explicitly capture temperature dependence based on the Arrhenius equation for nonisothermal processes (Bhattachar and Stouffer 1993), which states that the inelastic strain rate is proportional to the exponential of the dimensionless expression $\left(\frac{-Q}{KT}\right)$, as follows

$$\dot{\varepsilon}^I \, \alpha \exp\left(\frac{-Q}{KT}\right) \tag{11}$$

where Q is the activation energy, K is Boltzmann's constant, and T is the absolute temperature. By inserting the dimensionless expression $\left(\frac{-Q}{KT}\right)$ into the exponential term in the original expression for the components of the inelastic strain rate tensor (Bhattachar and Stouffer 1993), Equation (9), and defining a new state variable $\overline{Z}$ as

$$\overline{Z} = \frac{QZ}{K} \tag{12}$$

the new temperature-dependent components of the inelastic strain rate tensor can be expressed as

$$\dot{\varepsilon}_{ij}^I = \begin{cases} 2D_0 \exp\left[-\frac{1}{2}\left(\frac{\overline{Z}}{T\sigma_e}\right)^{2n}\right]\left(\frac{s_{ij}}{2\sqrt{J_2}} + A\delta_{ij}\right) & \text{if } \sigma_{kk} \neq 0 \text{ and } J_2 \neq 0 \\ 2D_0 \exp\left[-\frac{1}{2}\left(\frac{\overline{Z}}{T\sigma_e}\right)^{2n}\right]\left(\frac{s_{ij}}{2\sqrt{J_2}}\right) & \text{if } \sigma_{kk} = 0 \text{ and } J_2 \neq 0 \\ 2D_0 \exp\left[-\frac{1}{2}\left(\frac{\overline{Z}}{T\sigma_e}\right)^{2n}\right]\left(A\delta_{ij}\right) & \text{if } \sigma_{kk} \neq 0 \text{ and } J_2 = 0 \end{cases} \tag{13}$$

where $\overline{Z}$ is a temperature-dependent state variable that controls the resistance to internal stress at a given temperature, and the other parameters were defined previously. The components of the inelastic strain tensor are computed by integrating the components of the inelastic strain rate tensor (Eq. (13)). Even though polymers can exhibit large deformations, especially at low strain rates and at temperatures close to or above their glass transition temperature, infinitesimal strain theory has been assumed to apply, which permits the additive decomposition of the total strain tensor into its respective elastic, inelastic, and thermal components. This is justified because the intended application for the unified viscoplastic constitutive formulation is multiscale modeling of the high rate deformation of PMCs, where finite strains in the matrix are not expected. Based on the work of Bhattachar and Stouffer (1993) it is assumed that $\overline{Z}$ evolves in the same way as Z, that is,

$$\dot{\overline{Z}} = q\left(\overline{Z}_1 - \overline{Z}\right)\dot{\varepsilon}_e^I \tag{14a}$$

which can be integrated to yield

$$\bar{Z} = \bar{Z}_1 - \left(\bar{Z}_1 - \bar{Z}_0\right)\exp\left(-q\varepsilon_e^I\right) \tag{14b}$$

where $\bar{Z}_0$ and $\bar{Z}_1$ are the temperature-dependent initial and final values of $\bar{Z}$, respectively. Under isothermal conditions, Equations (14a) and (14b) are identical. However, under nonisothermal conditions, Equation (14b) should be used instead of Equation (14a) to allow the value of $\bar{Z}_0$ to change with temperature (Bhattachar and Stouffer 1993, Bhattachar 1991). It should be noted that the dimension of the hardening state variable Z is stress whereas the dimension of $\bar{Z}$ is stress times absolute temperature (Kelvin).

2.2 Bounds on Hydrostatic Constants

By examining Equation (7), it is apparent that the effective inelastic strain rate, $\dot{\varepsilon}_e^I$, is always nonnegative. Since the plastic work rate density (plastic dissipation) (Eq. (6)) must also be nonnegative (Chow and Lu 1989, Faria et al. 1998, Kawai et al. 2010), a relationship between γ and ξ must be determined to ensure the effective stress is also nonnegative. To this end, hydrostatic tensile and compressive load cases are considered. For hydrostatic tensile loading $\left(\boldsymbol{\sigma} = \mathrm{diag}\left(\left[\sigma, \sigma, \sigma\right]\right)\right)$, the effective stress is

$$\sigma_e = 3\sqrt{3\gamma}\sigma + 3\sqrt{3}\xi\sigma \geq 0 \tag{15}$$

For hydrostatic compressive loading $\left(\boldsymbol{\sigma} = \mathrm{diag}\left(\left[-\sigma, -\sigma, -\sigma\right]\right)\right)$, the effective stress is

$$\sigma_e = 3\sqrt{3\gamma}\sigma - 3\sqrt{3}\xi\sigma \geq 0 \tag{16}$$

According to Equations (15) and (16), the effective stress and plastic work rate density will always be nonnegative as long as the following condition is satisfied:

$$-\sqrt{\gamma} \leq \xi \leq \sqrt{\gamma} \tag{17}$$

2.3 Plastic Poisson's Ratios

To obtain physically realistic transverse plastic strains in uniaxial tensile and compressive loading, it is useful to derive expressions for the tensile and compressive plastic Poisson's ratios. For *uniaxial* loading in the 1-direction, the plastic Poisson's ratio for an isotropic material is defined as:

$$\nu^p = \frac{-\dot{\varepsilon}_{22}^I}{\dot{\varepsilon}_{11}^I} = \frac{-\dot{\varepsilon}_{33}^I}{\dot{\varepsilon}_{11}^I} = -\frac{\left(\dfrac{s_{22}}{2\sqrt{J_2}} + A\right)}{\left(\dfrac{s_{11}}{2\sqrt{J_2}} + A\right)} \tag{18}$$

Since the signs of the pressure and deviatoric stresses are opposite for uniaxial tensile and compressive loading, the tensile and compressive plastic Poisson's ratios, $\nu^{p,T}$ and $\nu^{p,C}$, can, in general, be different and are defined as follows:

$$\nu^{p,T} = -\frac{\left(\frac{s_{22}^{UT}}{2\sqrt{J_2}} + A_{UT}\right)}{\left(\frac{s_{11}^{UT}}{2\sqrt{J_2}} + A_{UT}\right)} = \frac{\sqrt{3} - 6A_{UT}}{2\sqrt{3} + 6A_{UT}} \tag{19a}$$

$$A_{UT} = \sqrt{\gamma} + \xi \tag{19b}$$

$$\nu^{p,C} = -\frac{\left(\frac{s_{22}^{UC}}{2\sqrt{J_2}} + A_{UC}\right)}{\left(\frac{s_{11}^{UC}}{2\sqrt{J_2}} + A_{UC}\right)} = \frac{\sqrt{3} + 6A_{UC}}{2\sqrt{3} - 6A_{UC}} \tag{20a}$$

$$A_{UC} = -\sqrt{\gamma} + \xi \tag{20b}$$

In Equations (19) and (20), "*UT*" denotes uniaxial tensile loading whereas "*UC*" denotes uniaxial compressive loading. By manipulating Equations (19a) and (20a), expressions for A_{UT} and A_{UC} in terms of the tensile and compressive plastic Poisson's ratios are obtained:

$$A_{UT} = \frac{-\left(s_{11}^{UT}\nu^{p,T} + s_{22}^{UT}\right)}{2\sqrt{J_2}\left(1+\nu^{p,T}\right)} = \frac{\sqrt{3} - 2\sqrt{3}\nu^{p,T}}{6\left(1+\nu^{p,T}\right)} \tag{21}$$

$$A_{UC} = \frac{-\left(s_{11}^{UC}\nu^{p,C} + s_{22}^{UC}\right)}{2\sqrt{J_2}\left(1+\nu^{p,C}\right)} = \frac{-\left(\sqrt{3} - 2\sqrt{3}\nu^{p,C}\right)}{6\left(1+\nu^{p,C}\right)} \tag{22}$$

To determine the bounds on the tensile and compressive plastic Poisson's ratios, consider Equations (17), (19b), and (20b). Equations (19b) and (20b) can be solved for ξ and $\sqrt{\gamma}$ to yield $\sqrt{\gamma} = \frac{1}{2}\left(-A_{UC} + A_{UT}\right)$ and $\xi = \frac{1}{2}\left(A_{UC} + A_{UT}\right)$. Combining Equations (19b) and (20b) with Equation (17) implies $A_{UC} \le 0$ and $A_{UT} \ge 0$, which imply, based on Equations (19a) and (20a), $\nu^{p,C} \le 0.5$ and $\nu^{p,T} \le 0.5$. By evaluating the limit of $\nu^{p,T}$ (Eq. (19a)) as A_{UT} tends to infinity and the limit of $\nu^{p,C}$ (Eq. (20a)) as A_{UC} tends to negative infinity, the lower bounds of the tensile and compressive plastic Poisson's ratios are obtained to be negative one (–1). Nonnegative plastic dissipation therefore implies $-1 < \nu^{p,C} \le 0.5$ and $-1 < \nu^{p,T} \le 0.5$. It is interesting to note that these are the same bounds as on the elastic Poisson's ratio for an isotropic material, except the tensile and compressive *plastic* Poisson's ratios can be equal to 0.5 (as is the case in deviatoric plasticity models) whereas the *elastic* Poisson's ratio cannot since it would result in an infinite bulk modulus. Note that for $0 \le \nu^{p,C} \le 0.5$ and $0 \le \nu^{p,T} \le 0.5$, $-\frac{\sqrt{3}}{6} \le \mathrm{A} \le \frac{\sqrt{3}}{6}$.

There are a several special cases of the model that merit a brief discussion. A pressure independent model is obtained by setting both hydrostatic constants equal to zero $\left(\gamma = \xi = 0\right)$. In this case, the effective stress reduces to the von Mises effective stress $\left(\sqrt{3J_2}\right)$, which implies the plastic deformation is deviatoric (tensile and compressive plastic Poisson's ratios are equal to 0.5) and the magnitudes of the tensile and compressive saturation stresses are equal. The model used in previous research (Sorini et al. 2019) is obtained by setting γ equal to zero $\left(\xi \neq 0\right)$; this should not be done, as the model will inherit the same deficiencies as the original model (Goldberg et al. 2005, Sorini et al. 2019). A pressure-dependent model that does not exhibit tension-compression asymmetry is obtained by setting ξ equal to zero $\left(\gamma \neq 0\right)$. In this case, magnitudes of the tensile and compressive saturation stresses as well as the plastic Poisson's ratios are equal; $\gamma \geq 0$ ensures $-1 < \nu^{p,C} \leq 0.5$ and $-1 < \nu^{p,T} \leq 0.5$ whereas $0 \leq \gamma \leq \frac{1}{12}$ ensures $0 \leq \nu^{p,C} \leq 0.5$ and $0 \leq \nu^{p,T} \leq 0.5$.

2.4 Tension-Compression Asymmetry

Plasticity formulations that employ plastic potential functions that are even functions of hydrostatic pressure are incapable of simulating tension-compression asymmetry. For tension-compression asymmetry, the value of the effective stress in uniaxial tension should be greater than the value of the effective stress in uniaxial compression *for the same absolute value of applied uniaxial stress*. In other words, a greater uniaxial stress would need to be applied in compression, σ^{UC}, than in tension, σ^{UT}, to achieve equivalent values of the effective stress. Using Equation (5), this can be expressed as:

$$\sigma_e = \sigma^{UT}\left(1 + \sqrt{3}A_{UT}\right) = \sigma^{UC}\left(1 - \sqrt{3}A_{UC}\right) \tag{23}$$

Therefore, for tension-compression asymmetry $\left(\sigma^{UC} > \sigma^{UT}\right)$, $A_{UC} > -A_{UT}$, which implies the hydrostatic constant $0 < \xi \leq \sqrt{\gamma}$.

2.5 Summary of Constraints on Model Parameters and Special Cases

The conditions for nonnegative plastic dissipation, tension-compression asymmetry, and model special cases are summarized in Table I.

TABLE I.—CONDITIONS FOR NONNEGATIVE PLASTIC DISSIPATION, TENSION-COMPRESSION ASYMMETRY, AND MODEL SPECIAL CASES

Condition	Remark
$-\sqrt{\gamma} \leq \xi \leq \sqrt{\gamma}$	Nonnegative plastic dissipation
$0 < \xi \leq \sqrt{\gamma}$	Nonnegative plastic dissipation and tension-compression asymmetry
$\xi = \sqrt{\gamma}$	Plastically incompressible in compression
$\xi = \gamma = 0$	Pressure independent model; deviatoric plastic strain tensor; equal uniaxial tensile and compressive saturation stresses
$\gamma \neq 0,\ \xi = 0$	Pressure dependent model with no tension-compression asymmetry
$\gamma = 0,\ \xi \neq 0$	Deficient model; possibility of negative plastic work and plastic Poisson's ratios that are out of bounds

2.6 Adiabatic Heating

The heat energy equation, which expresses the relationship between mechanical deformation and spatial-temporal temperature change, is as follows

$$k\nabla^2 T - \alpha_M (3\lambda + 2\mu) T\dot{\varepsilon}^e_{kk} + \beta\boldsymbol{\sigma} : \dot{\boldsymbol{\varepsilon}}^{\boldsymbol{I}} = \rho C\dot{T} \tag{24}$$

where k is the thermal conductivity, T is the temperature, α_M is the coefficient of thermal expansion, λ and μ are Lame's constants, $\dot{\varepsilon}^e_{kk}$ is the elastic volumetric strain rate, $\boldsymbol{\sigma}$ is the Cauchy stress tensor, $\dot{\boldsymbol{\varepsilon}}^{\boldsymbol{I}}$ is the inelastic strain rate tensor, ρ is the density, C is the specific heat, and β is the inelastic heat fraction, which represents the fraction of inelastic work converted to heat. As aforementioned, the intended application of the unified viscoplastic constitutive formulation is the multiscale analysis of PMCs subjected to impact loading, where adiabatic conditions can generally be assumed to prevail (Li and Lambros 2001, Kendall and Siviour 2013, Trojanowski 1997, Garg et al. 2008, Chou et al. 1973). As in previous work by the authors (Sorini et al. 2019), it is useful to derive a characteristic thermal diffusion time to justify the assumption of adiabatic conditions for high rate loading. To this end, consider the one-dimensional heat (diffusion) equation:

$$k\frac{\partial^2 T}{\partial \mathrm{x}^2} = \rho C\frac{\partial T}{\partial t} \tag{25}$$

By replacing the partial derivatives in Equation (25) with finite differences, the following expression is obtained for the characteristic thermal diffusion time, Δt_d,

$$\Delta t_d = \frac{(\Delta x)^2}{D} \tag{26}$$

where D is the thermal diffusivity $\left(D = \frac{k}{\rho C}\right)$ and Δx is a characteristic length, which can be taken as the distance between the center of the deforming region of a test specimen and the nearest heat sink (Arruda et al. 1995). If the time of a given experiment is small compared to the characteristic thermal diffusion time, adiabatic conditions can be assumed to prevail and the conduction term in Equation (24) can be neglected. The characteristic thermal diffusion time can also be used to compute an *approximate* strain rate at which the system would be expected to behave adiabatically, Δt_d^{-1}. More details regarding the characteristic thermal diffusion time for E862 resin are given in Section 4.0. The thermoelastic term in Equation (24) is often negligible compared to the thermoplastic term (Li and Lambros 2001, Varghese and Batra 2009, Pan et al. 2016, Siviour and Jordan 2016), reducing the heat energy equation to

$$\beta\boldsymbol{\sigma} : \dot{\boldsymbol{\varepsilon}}^{\boldsymbol{I}} = \rho C\dot{T} \tag{27}$$

Assuming the inelastic heat fraction, β, is known, either measured experimentally or assumed, Equation (27) can be integrated to compute the temperature change due to the conversion of plastic work to heat at each timestep in an incremental solution procedure.

2.7 Temperature Dependence of Elastic Properties

A time-temperature shifting methodology, similar to the Decompose-Shift-Reconstruct (DSR) method originally developed by Mulliken and Boyce (2006), is utilized to compute temperature and strain rate dependent shifts in elastic moduli based on dynamic mechanical analysis (DMA) tests conducted on neat resin at various frequencies. The frequency at which a DMA test is conducted corresponds to a particular strain rate (depending on the specimen geometry), therefore rate-dependent shifts in the shear storage modulus can be obtained by conducting DMA tests in shear at various frequencies and performing a temperature sweep. A schematic of the shifting of the shear storage modulus versus temperature curve with strain rate is shown in Figure 1 for E862 epoxy DMA data (Gilat et al. 2007). It is interesting to note that the glass transition temperature is rate dependent, increasing with increasing strain rate (Mulliken and Boyce 2006). In this research, it is assumed that the shear modulus is equal to the shear storage modulus. Assuming the elastic Poisson's ratio is independent of temperature and strain rate (Mulliken and Boyce 2006, Jordan et al. 2008, Varghese and Batra 2009), the shifting of the DMA data allows the elastic properties to be determined at various strain rates (can also be extrapolated to higher/lower strain rate values than those at which the DMA tests were conducted) and temperatures.

To perform the horizontal (temperature direction) shifting of the shear storage modulus versus temperature curve with strain rate, it is necessary to determine a reference strain rate, $\dot{\bar{\varepsilon}}_{ref}$, with respect to which the shifting occurs. Since the DMA shear storage modulus versus temperature curve for E862 presented in Gilat et al. (2007) corresponds to a strain rate of 0.02/s, this value has been taken as the reference strain rate. To perform the shifting numerically, the logarithm of the ratio of the actual strain rate to the reference strain rate, the "log strain rate ratio", must be computed and multiplied by the "DMA shift factor". The log strain rate ratio quantifies the number of decades the actual strain rate is above or below the reference strain rate. For example, an actual strain rate of 0.2/s is ten times greater than the reference strain rate; the logarithm of ten is one (i.e., 0.2/s is one decade higher than 0.02/s). The DMA shift factor quantifies how much the shear storage modulus versus temperature curve shifts horizontally per decade change in strain rate with respect to the reference strain rate. Since a tabular approach has been taken, the value of the DMA shift factor must be determined via trial and error during the calibration procedure. In previous work (Sorini et al. 2019), a DMA shift factor of 10 K per decade strain rate was

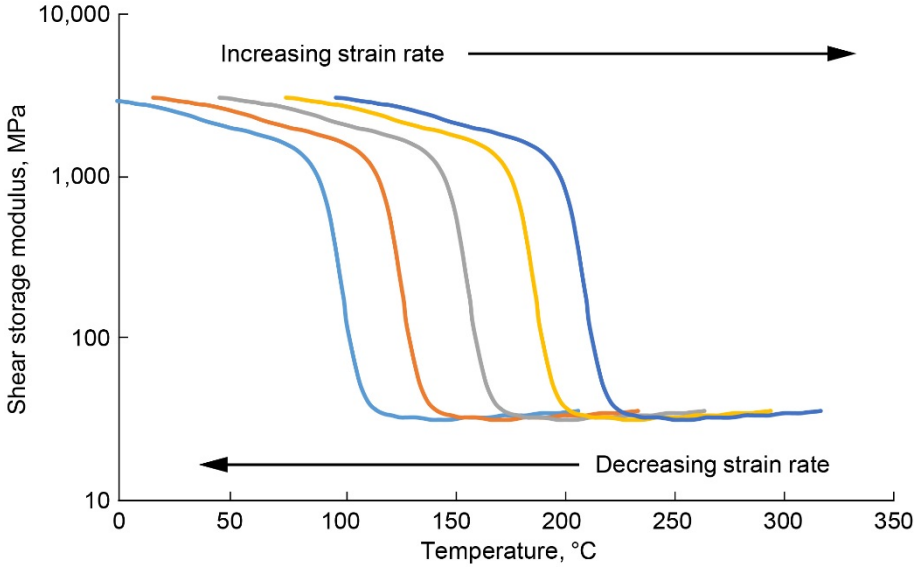

Figure 1.—Illustration of shifting of Epon 862 epoxy DMA data with strain rate.

used for the E862 resin; in this work, a DMA shift factor of 5 K per decade strain rate was found to more accurately match experimental test data. If DMA data is unavailable, it is recommended to at least approximate the rate and temperature dependence of the elastic modulus of the material of interest. This can be done by measuring the elastic properties over a range of temperatures and strain rates and determining an approximate functional dependence of the moduli on rate and temperature. The reader is referred to Richeton et al. (2007) for an example of an analytical description of the rate and temperature and dependence of the elastic moduli. It should also be noted that, if the unified viscoplasticity formulation is implemented into a finite element code as a user defined material subroutine, a strain rate below which no shifting of the shear storage modulus versus temperature curve occurs should be defined. This is because, at least in explicit finite element simulations integration point effective strain rates will be zero until deformation occurs. Since the limit of the logarithm function as its argument approaches zero is negative infinity, a strain rate of zero would result in a shift factor of negative infinity, which would cause numerical problems.

2.8 Model Calibration

The polymer constitutive model requires determining five constants $\left(D_0, n, q, \gamma, \text{and } \xi\right)$ and two functions of temperature, $\bar{Z}_0\left(T\right)$ and $\bar{Z}_1\left(T\right)$. The characterization procedure is similar to that presented in Sorini et al. (2019) and is based on neat resin isothermal test data at different temperatures. As in previous research (Sorini et al. 2019, Goldberg et al. 2005), the value of D_0 is taken to be 1×10^6/s. Since there are no hydrostatic stresses in pure shear deformation of an isotropic material, the initial calibration is based on pure shear test data. The values of n and $\bar{Z}_1$ at a given temperature are determined as follows using Equation (13), simplified for the case of pure shear loading $\left(J_2=\tau^2;\ \sigma_e=\sqrt{3}|\tau|\right)$:

$$\dot{\varepsilon}^I=\frac{\dot{\gamma}^I}{2}=D_0\exp\left(-\frac{1}{2}\left(\frac{\bar{Z}\left(T\right)}{\sqrt{3}|\tau|T}\right)^{2n}\right)\left(\frac{\tau}{|\tau|}\right) \tag{28}$$

where $\dot{\gamma}^I$ is the inelastic engineering shear strain rate. Equation (28) is then manipulated to yield:

$$\ln\left(-2\ln\left(\frac{\dot{\gamma}^I}{2D_0}\right)\right)=2n*\ln\left(\bar{Z}\left(T\right)\right)-2n*\ln\left(\sqrt{3}|\tau|T\right) \tag{29}$$

To obtain the value of the constant n and $\bar{Z}_1$ at a particular temperature, constant strain rate pure shear tests at various strain rates (ideally at least three) at the temperature of interest are used. The value of the saturation shear stress, τ_s, (the stress level where the stress-strain curve flattens out) is then substituted in for τ in Equation (29). Since at saturation, the inelastic strain rate is equal to the total strain rate, the value of the inelastic engineering shear strain rate, $\dot{\gamma}^I$, is set equal to the total applied engineering shear strain rate, $\dot{\gamma}_0$. For each available shear stress-strain curve, data pairs of the total applied engineering shear strain rate and the corresponding saturation shear stress (one pair for each curve) are used. The values of the absolute test temperature and the constant D_0 are also inserted into Equation (29). Least squares regression is then performed on the data pairs of engineering shear strain rates and corresponding saturation shear stresses for each test. The value of $\bar{Z}$ is taken to be the value at saturation, $\bar{Z}_1$. As

evident from Equation (29), the slope of the line of best fit is equal to –2*n* and the intercept is equal to $2n * \ln\left(\bar{Z}_1(T)\right)$. The values $\bar{Z}_1$ for a given temperature and *n* are now known. The aforementioned process is repeated for pure shear tests at various rates at other temperatures to determine the temperature-dependence of $\bar{Z}_1$. In this research, *n* is assumed to be constant, however a possible inverse relationship between *n* and temperature (i.e., higher rate sensitivity for higher temperatures) has been suggested (Bodner 2001).

To obtain the value of $\bar{Z}_0$ at a particular temperature, Equation (28) is rearranged as follows:

$$\bar{Z}(T) = \left[-2\ln\left(\frac{\dot{\gamma}^I}{2D_0} \right) \right]^{\frac{1}{2n}} \sqrt{3}|\tau|T \tag{30}$$

The values of shear stress and corresponding inelastic engineering shear strain rate where the shear stress-strain curves deviate from linearity are used in Equation (30) for the values of τ and $\dot{\gamma}^I$, respectively. One hundredth of the constant strain rate used in the test has been found by trial and error to be a good approximation the value of $\dot{\gamma}^I$ (Sorini et al. 2019, Goldberg et al. 2005). Equation (30) is then evaluated for $\bar{Z}$, which is set equal to $\bar{Z}_0$. This procedure is repeated for multiple temperatures to determine the temperature-dependence of $\bar{Z}_0$.

To determine the value of *q* for Equations (14a) and (14b), Equation (14a) is integrated for the case of pure shear loading, yielding

$$\bar{Z}(T) = \bar{Z}_1(T) - \left(\bar{Z}_1(T) - \bar{Z}_0(T)\right)\exp\left[\frac{-q}{\sqrt{3}}\gamma^I \right] \tag{31}$$

where γ^I is the engineering shear strain. At saturation, $\bar{Z}(T)$ approaches $\bar{Z}_1(T)$ and the exponential term approaches zero. As in previous work (Sorini et al. 2019, Goldberg et al. 2005), it is assumed saturation occurs when the following condition is satisfied

$$\exp\left[\frac{-q}{\sqrt{3}}\gamma_s^I \right] = 0.01 \tag{32}$$

where γ_s^I is the inelastic shear strain at saturation. This determines the value of the hardening rate *q*.

To determine the values of the hydrostatic constants, γ and ξ, uniaxial tensile and compressive test data are used. Ideally, one would measure the tensile and compressive plastic Poisson ratios in the tensile and compressive tests using digital image correlation (DIC) and use Equations (21) and (22) to determine the values of A_{UT} and A_{UC}. The values of A_{UC} and A_{UT} would then be used in Equations (19b) and (20b) to determine the values of the hydrostatic constants:

$$\begin{bmatrix} -1 & 1 \\ 1 & 1 \end{bmatrix}\begin{bmatrix} \sqrt{\gamma} \\ \xi \end{bmatrix} = \begin{bmatrix} A_{UC} \\ A_{UT} \end{bmatrix} \rightarrow \begin{bmatrix} \sqrt{\gamma} \\ \xi \end{bmatrix} = \frac{1}{2}\begin{bmatrix} -1 & 1 \\ 1 & 1 \end{bmatrix}\begin{bmatrix} A_{UC} \\ A_{UT} \end{bmatrix} \tag{33}$$

However, it is well known that, after the peak load, plastic instabilities (necking in tension and barreling in compression) cause nonuniform stress and strain states in the gage section (Poulain et al. 2013, Poulain et al. 2014) and, thus, the plastic Poisson's ratios are likely not material constants (Kolling et al.

2005). The plastic Poisson's ratios may change with temperature, strain rate, and the level of deformation. However, to keep the constitutive model tractable, the tensile and compressive plastic Poisson's ratios are assumed to be constant in this research. If it is found that the characterization is precluded by the assumption of constant plastic Poisson's ratios, evolution equations for the hydrostatic parameters, similar to those in previous work (Sorini et al. 2019, Goldberg et al. 2005), can be used, though care should be taken to ensure the constraints derived in Section 2.2 are satisfied. If information regarding the permanent volume change in uniaxial tensile and compressive tests is available, this information can be used to facilitate the determination of the hydrostatic constants as well. For example, if there was no permanent volume change in a uniaxial compression test, it suggests a compressive plastic Poisson's ratio of 0.5 (plastically incompressible in compression). If values of the tensile and compressive plastic Poisson's ratios are unavailable, it can be assumed that the effective stresses (Eq. (5)) at saturation in shear, tension, and compression are equal for a given strain rate and temperature (i.e., the shear, tension, and compression tests should be conducted at approximately the same temperature and strain rate). This results in the following two equations

$$\sqrt{3}\tau_s = \sigma_{st}\left(1+\sqrt{3\gamma}+\sqrt{3}\xi\right) \tag{34}$$

$$\sqrt{3}\tau_s = \sigma_{sc}\left(1+\sqrt{3\gamma}-\sqrt{3}\xi\right) \tag{35}$$

where τ_s, σ_{st}, σ_{sc} are the shear, tensile, and compressive stresses at saturation, respectively. It is evident that, for a pressure independent material $\left(\gamma=\xi=0\right)$, the well-known relation between the shear, tensile, and compressive stresses at saturation is obtained: $\sqrt{3}\tau_s = \sigma_{st} = \sigma_{sc}$. By inserting the saturation values of the experimental shear, tensile, and compressive stresses, Equations (34) and (35) can be solved for the two unknown hydrostatic constants, γ and ξ. The values of these constants are assumed to be independent of rate and temperature, so the results from tests at one strain rate and temperature are sufficient to find the necessary values. Note that in this model, for a given strain rate and temperature, the larger the tensile and/or compressive plastic Poisson's ratio, the larger the magnitude of the tensile and/or compressive saturation stresses. Thus, the maximum tensile and compressive (absolute value) saturation stresses for a given strain rate and temperature are therefore obtained for plastic Poisson's ratios of 0.5.

3.0 Micromechanics

To predict the effective behavior of a unidirectional composite, including the effects of local matrix adiabatic heating and subsequent thermal softening, the unified viscoplastic formulation is used as a constitutive model in the GMC micromechanics framework (Aboudi et al. 2012, Paley and Aboudi 1992, Pindera and Bednarcyk 1999). By assuming first order subcell displacement field and enforcing displacement and traction continuity conditions between adjacent subcells and adjacent unit cells, GMC can predict the effective response of a unidirectional composite based on the properties, volume fractions, and arrangement of the constituents. The formulation used in this work is based on the reformulated GMC described in (Aboudi et al. 2012). In the micromechanics model, the microscale repeating unit cell (RUC) consists of four subcells: three matrix and one fiber. A schematic of the microscale RUC is shown in Figure 2. Fibers are assumed to exhibit linear elastic constitutive behavior whereas the plastically dilatant unified viscoplastic polymer model described in Section 2.0 is applied to the matrix subcells.

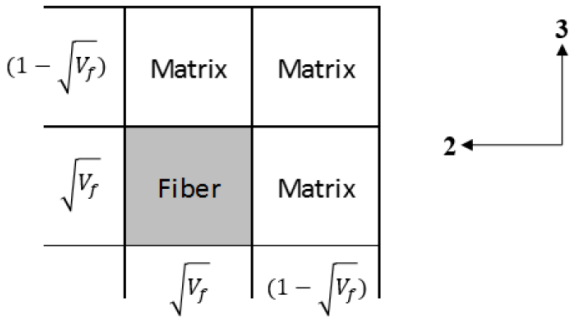

Figure 2.—Schematic of four subcell RUC for GMC micromechanics analysis.

4.0 Results

4.1 Response of Monolithic Polymer

To demonstrate the capability of the modified constitutive model, it is calibrated for E862 epoxy using available data (Gilat et al. 2007, Littell 2008, Littell et al. 2008) from tension, compression and shear tests conducted over a range of strain rates and temperatures. In this section, the 620/s tensile curves are from Gilat et al. (2007) whereas the rest of the data is from Littell (2008) and Littell et al. (2008). This is the same experimental data used to characterize the viscoplastic model used in previous work by the authors (Sorini et al. 2019). Note that all tests used for characterization were conducted below the E862 glass transition temperature reported by Gilat et al. (2007), 133 °C, which was determined from a DMA test conducted in shear at 10 rad/s (0.02/s). The experimental E862 stress-strain data presented in Littell (2008) and Littell et al. (2008) is in terms of engineering stress and a local strain determined by averaging digital image correlation (DIC) measurements at several points in the middle of the specimen gage sections (Littell 2008, Poulain et al. 2013). In previous work, based on DIC data provided by the authors of Littell et al. (2008), the true stress in the uniaxial tension and compression tests, σ^{true}, was computed from the corresponding engineering stress, σ^{eng}, using Equation (36)

$$\sigma^{\text{true}} = \frac{\sigma^{\text{eng}}}{\left(1+\varepsilon_T^{\text{eng}}\right)^2} \tag{36}$$

where ε_T is the transverse *engineering* strain measured by the DIC in the tension and compression tests. However, in previous work, the DIC strains presented in Littell (2008) and Littell et al. (2008) were assumed to be the *true* strains. In this work, the true stresses were therefore recomputed using the following equation (Poulain et al. 2013):

$$\sigma^{\text{true}} = \frac{\sigma^{\text{eng}}}{\exp\left(2\varepsilon_T^{\text{true}}\right)} \tag{37}$$

where $\varepsilon_T^{\text{true}}$ is the transverse *true* strain measured by the DIC in the tension and compression tests. Since the relationship between longitudinal and transverse true strain for uniaxial loading is $\varepsilon_T^{\text{true}} = -\nu\varepsilon_L^{\text{true}}$ and the relation between engineering and true normal strain is $\varepsilon^{\text{true}} = \ln\left(\varepsilon^{\text{eng}}+1\right)$, the relationship between

the longitudinal and transverse engineering strain for uniaxial loading is $\left(1+\varepsilon_T^{\text{eng}}\right)=\left(1+\varepsilon_L^{\text{eng}}\right)^{-\nu}$ (Arnold et al. 2019). It is therefore evident that, for a Poisson's ratio of 0.5, Equations (36) and (37) reduce to the well-known conversions between true and engineering stress, $\sigma^{\text{true}}=\sigma^{\text{eng}}\left(1+\varepsilon_L^{\text{eng}}\right)=\sigma^{\text{eng}}\exp\left(\varepsilon_L^{\text{true}}\right)$, which assume incompressibility. The uniaxial tensile and compressive stress-strain curves computed using Equations (36) and (37) are nearly identical and are shown in Figure 12 and Figure 13 in the Appendix. The shear test data presented in Littell (2008) and Littell et al. (2008) was unmodified.

The resin material properties and model parameters used in the simulations are presented in Table II. To illustrate how the values of the hydrostatic constants were obtained, consider the room temperature shear, tension, and compression data presented in Figure 3(a), Figure 4(a), and Figure 5(a). The saturation stresses for the shear, tension, and compression tests conducted at strain rates of 1.6×10^{-1}/s, 1×10^{-1}/s, and 1×10^{-1}/s are 64.99, 103.83, and 112.23 MPa, respectively. Using these values in Equations (34) and (35) yields tensile and compressive plastic Poisson's ratios of 0.3836 and 0.4955. These values were *slightly* adjusted manually to obtain an optimal fit with the shear, tension, and compression test data at the various other test temperatures and strain rates; the values of γ and ξ in Table II correspond to tensile and compressive plastic Poisson's ratios of 0.3827 and 0.5, respectively. Note that the modulus values presented in Table II are slightly different than in previous research (Sorini et al. 2019) because, as aforementioned, a DMA shift factor of 5 K per decade strain rate was used in this research (10 K per decade strain rate was used in the previous work).

In the simulations presented in this section, the inelastic heat fraction has been set to zero (no adiabatic heating) since i) many of the experiments were conducted at low strain rates, where adiabatic heating due to the conversion of plastic work to heat can be assumed to be negligible and ii) the available high strain rate test data exhibited fairly low failure strains, where the material response displayed minimal nonlinearity, and thus likely limited adiabatic heating due to plastic deformation. As in previous work (Sorini et al. 2019), using Equation (26), E862 material properties $\rho=1,200\frac{\text{kg}}{\text{m}^3}$ (Littell 2008), $k=0.18\frac{\text{W}}{\text{m-K}}$ (Spurgeon 2018), $C=1,260\frac{\text{J}}{\text{kg-K}}$ (Rowghanian and Hoa 2011), and assuming the characteristic length, Δx, is equal to half of the initial test coupon gage length used in the E862 neat resin tests presented in Littell (2008) and Littell et al. (2008) ($\Delta x=1.5875\,\text{mm}$, which is also equal to the initial test coupon gage radius), the characteristic thermal diffusion time is found to be 21.17 sec. The corresponding *approximate* strain rate at which the system would be expected to behave adiabatically, Δt_d^{-1}, is 0.047/s. Note that this approximation does not account for the temperature dependence of the thermal properties of the material or the fact that the characteristic length, Δx, changes throughout the deformation. Additionally, in reality, the transition from roughly isothermal to roughly adiabatic conditions spans a range of strain rates. Garg et al. (2008) conducted uniaxial compression tests on E862 and found experimentally that, for their cubic specimens of 5 and 10 mm side lengths, a strain rate of 0.5/s provided approximately adiabatic conditions. However, using the thermal properties mentioned above, Equation (26), and considering the characteristic length to be half the side length of the cubic specimens used by Garg et al. (2008), the approximate transition strain rates for the 5 and 10 mm side length specimens are 0.019 and 0.0048, respectively, which are roughly 26 and 104 times less than 0.5/s. This implies that the strain rate at which the E862 tests presented in Littell (2008) and Littell et al. (2008) could actually be between 1.2 and 4.9/s. It is therefore reasonable to assume isothermal conditions for the simulations in this section. The fact that Garg et al. (2008) observed approximately adiabatic conditions at

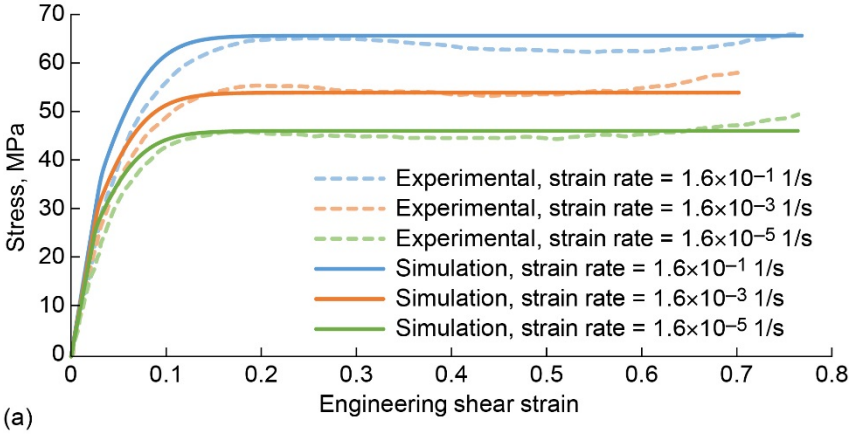

(a)

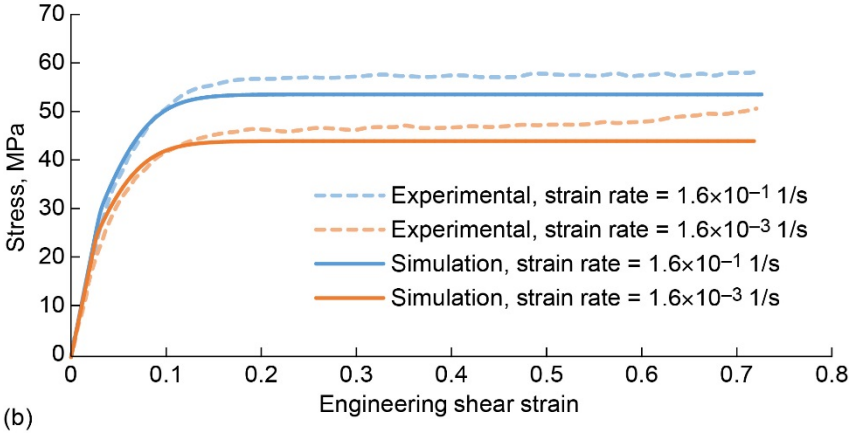

(b)

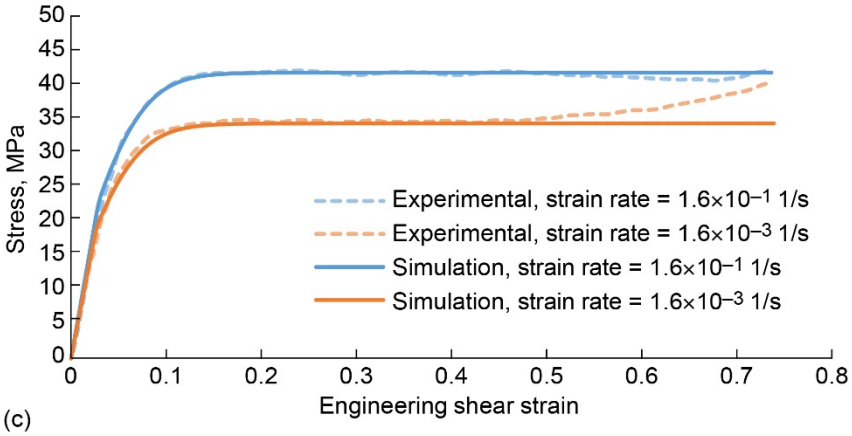

(c)

Figure 3.—Simulated and experimental shear stress-strain response of Epon 862 epoxy at (a) Room temperature (25 °C); (b) 50 °C; (c) 80 °C.

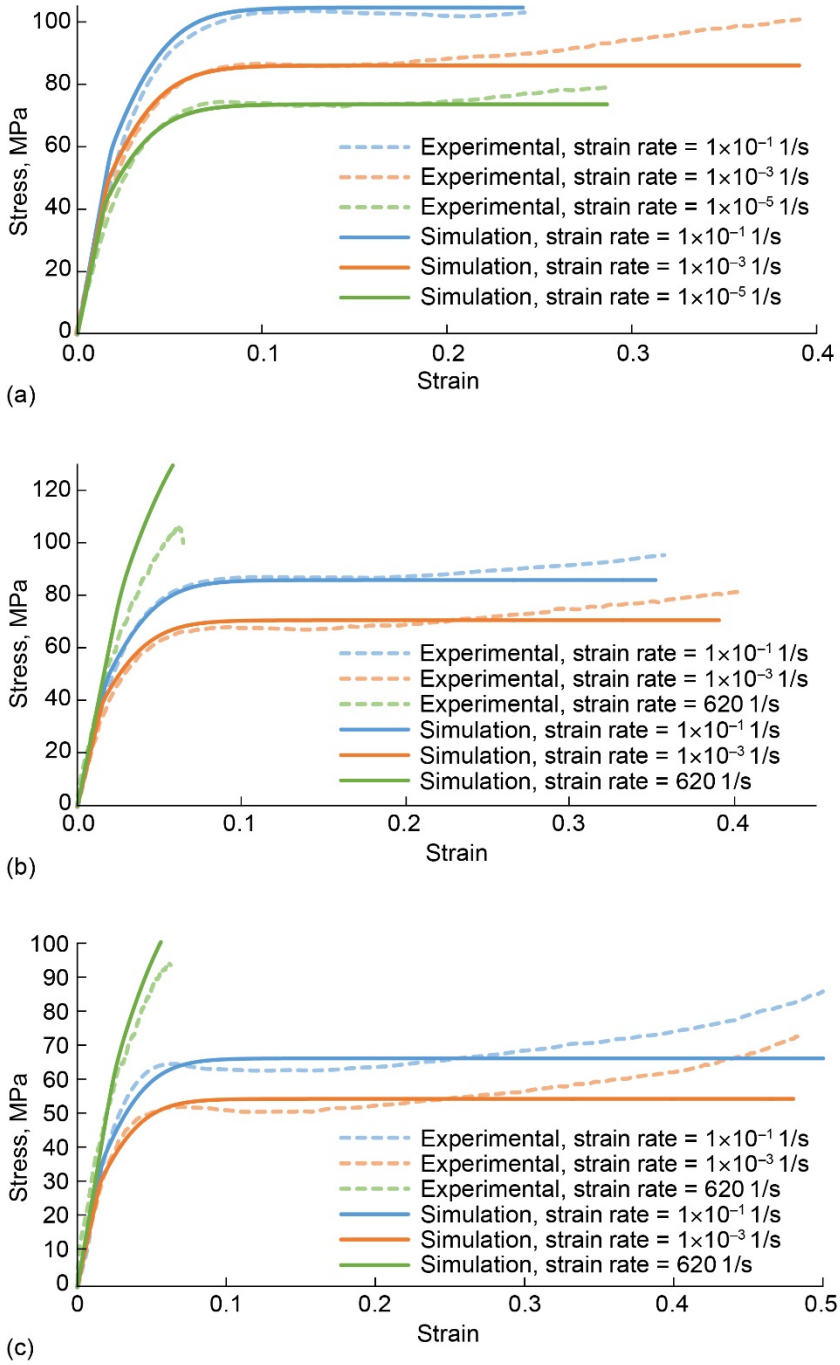

Figure 4.—Simulated and experimental tensile stress-strain response of Epon 862 epoxy at (a) Room temperature (25 °C); (b) 50 °C; (c) 80 °C.

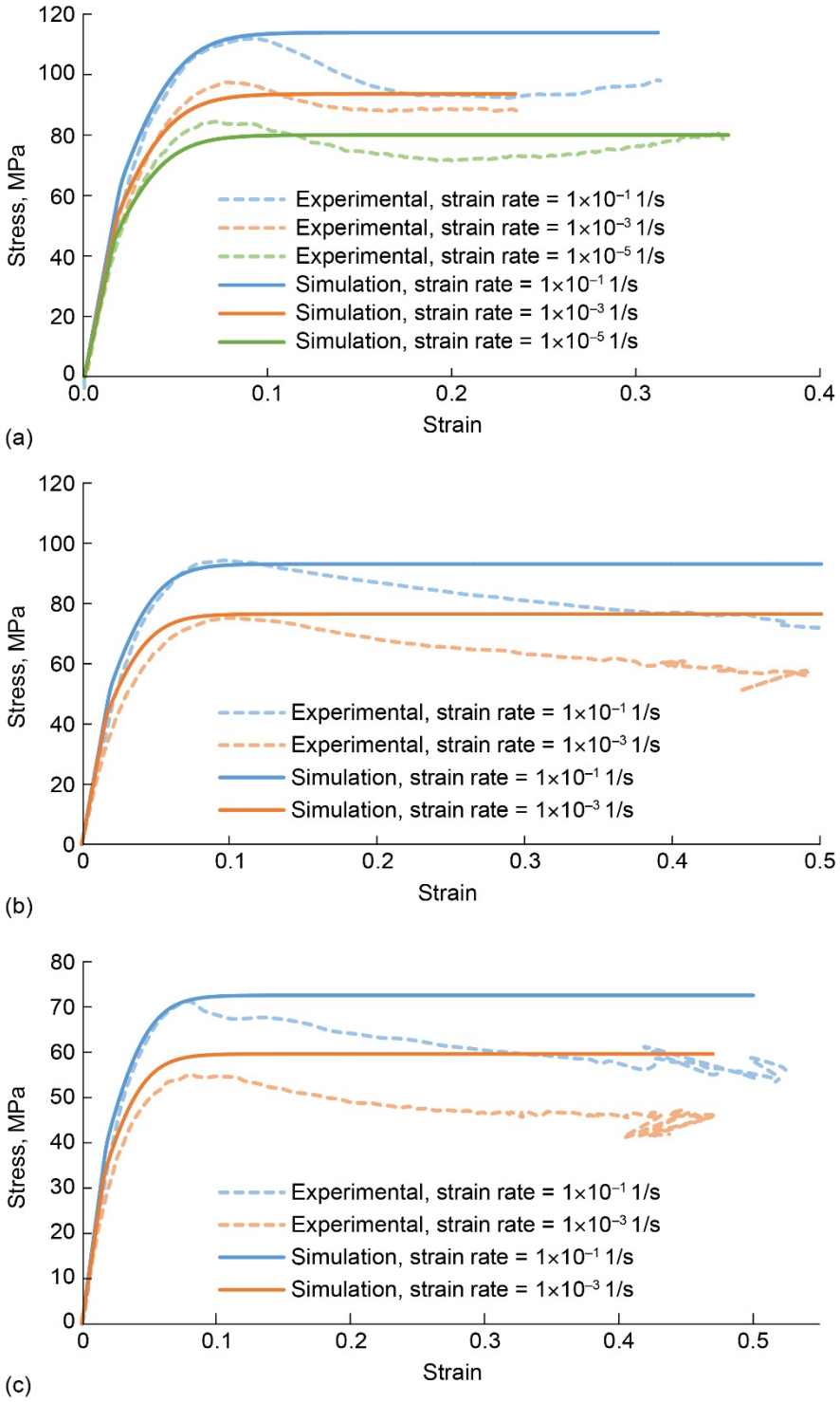

Figure 5.—Simulated and experimental compressive stress-strain response of Epon 862 epoxy at (a) Room temperature (25 °C); (b) 50 °C; (c) 80 °C.

a strain rate of 0.5/s helps to further justify the adiabatic assumption for dynamic loading, such as impact events, where much larger strain rates are expected. Note that Poulain (2010) has suggested that the post-peak softening observed in the E862 compression response (Littell 2008 and Littell et al. 2008) is intrinsic material behavior, not thermal softening.

Figure 3, Figure 4, and Figure 5 show the simulated and experimental shear, tensile, and compressive stress-strain response of E862 epoxy resin at room temperature (25 °C), 50 °C, and 80 °C for various strain rates. Reasonably good correlations with experimental data are obtained for all the strain rates and temperatures for shear, tensile and compressive loading. Based on the characterization, it was found that $\overline{Z}_0$ and $\overline{Z}_1$ approximately decrease linearly with temperature, as shown in Table II, which is why the model slightly underestimates the shear saturation stresses at 50 °C (Figure 3(b)). Due to the significant change in elastic properties above the glass transition temperature, it is likely that $\overline{Z}_0$ and $\overline{Z}_1$ would exhibit a different functional dependence than shown in Table II near and above the glass transition. Therefore, modeling $\overline{Z}_0$ and $\overline{Z}_1$ as piecewise functions of temperature or using a tabular approach may be more appropriate. Regardless of the method used to model the temperature dependence of $\overline{Z}_0$ and $\overline{Z}_1$, these functions must decrease with temperature (resistance to internal stress decreases as temperature increases). Care should also be taken to ensure $\overline{Z}_0$ and $\overline{Z}_1$ are always positive and that $\overline{Z}_1$ is always greater than $\overline{Z}_0$ for temperature ranges of interest; this may require setting these parameters to be constant for very high temperatures. It can be seen in Figure 5(a)) that the room temperature saturation stresses in the 1×10^{-3}/s and 1×10^{-5}/s strain rate compression simulations are slightly lower than the experimental values. This is interesting because the compressive plastic Poisson's ratio in the model is 0.5 and therefore the compressive saturation stresses are the highest they can possibly be (since the saturation stress increases with plastic Poisson's ratio and 0.5 is the upper bound). Figure 5(c) shows that the 80 °C saturation stress in the 1×10^{-3}/s strain rate compression simulation is slightly higher than the experimental value. This could suggest a nonconstant compressive plastic Poisson's ratio. As evident in Figure 3,

TABLE II.—EPON 862 MATERIAL PROPERTIES AND MODEL PARAMETERS

<table>
<tr><td>Young's Modulus</td><td colspan="2">*Taken from DMA curve (Figure 1)*</td><td colspan="3">Temperature (°C)</td></tr>
<tr><td rowspan="4"></td><td rowspan="4">Rate (1/s)</td><td></td><td>30</td><td>50</td><td>80</td></tr>
<tr><td>1×10^{-3}</td><td>2.90</td><td>2.58</td><td>2.00</td></tr>
<tr><td>1</td><td>3.27</td><td>2.81</td><td>2.29</td></tr>
<tr><td>1,000</td><td>3.65</td><td>3.14</td><td>2.58</td></tr>
<tr><td>Poisson's Ratio</td><td colspan="5">0.4</td></tr>
<tr><td>Density (kg/m^3)</td><td colspan="5">1,200</td></tr>
<tr><td>Specific Heat (J/kg-K)</td><td colspan="5">1,260</td></tr>
<tr><td>CTE (1/K)</td><td colspan="5">5.4×10^{-5}</td></tr>
<tr><td>D_0 (1/s)</td><td colspan="5">1×10^{6}</td></tr>
<tr><td>n</td><td colspan="5">0.6351</td></tr>
<tr><td>q</td><td colspan="5">74.4073</td></tr>
<tr><td>γ</td><td colspan="5">$6\text{x}10^{-4}$</td></tr>
<tr><td>ξ</td><td colspan="5">0.02449</td></tr>
<tr><td>$\overline{Z}_0(T)$(Pa-K)</td><td colspan="5">$-(1.462\times10^{9})T+7.421\times10^{11}$</td></tr>
<tr><td>$\overline{Z}_1(T)$(Pa-K)</td><td colspan="5">$-(2.365\times10^{9})T+1.232\times10^{12}$</td></tr>
</table>

Figure 4, and Figure 5, the model does not simulate the intrinsic strain softening observed in the compressive material response or the second hardening observed in the tensile and compressive response at very high strains. This is assumed to be acceptable since the matrix in PMCs will likely fail at small strains before these effects become significant.

Figure 6(a) to (c) show the effect of varying the inelastic heat fraction between zero and unity for shear, tensile, and compressive loading at a strain rate of 1,000/s and an initial temperature of 25 °C. Higher temperature rises, resulting in more thermal softening, are observed for higher inelastic heat fractions for all loading cases, as expected.

To demonstrate the improvements made to the Goldberg (Goldberg et al. 2005) model, the response of the improved model is compared to the Goldberg model at 25 °C. All the Goldberg model parameters are identical to those in the improved model, except Z_0, Z_1, and the hydrostatic constants. In the Goldberg model, the components of the inelastic strain rate tensor components are not temperature dependent. Therefore, the values of $Z_0(T)$ and $Z_1(T)$ in the Goldberg model are equal to those in the improved model divided by the absolute temperature. Additionally, since the Goldberg model employs a single hydrostatic state variable, α, its initial and final values have been set equal to the value of A_{UT} (0.049), which results in constant plastic Poisson's ratios.

Figure 7 shows the stress and total Poisson's ratio predicted by the improved model and the Goldberg model as a function of strain in the load direction for simulated uniaxial tensile and compressive loading at 1,000/s and 25 °C. In Figure 7(a), the tensile saturation stresses are the same, but the compressive saturation stresses are different. This implies that the Goldberg model is capable of simulating the same response as the improved model in tension and shear, but not in compression. Figure 7(b) shows the *total* Poisson's ratios in tension and compression for both models. The Poisson's ratios start at their elastic values (0.4) and, in the case of the improved model, approach their plastic values as the deformation progresses. However, in the Goldberg model predictions the compressive Poisson's ratios exceeds 0.5.

The following illustrates the importance of the fact that A, $\sqrt{\gamma}\,\mathrm{sign}(\sigma_{kk})+\xi$, changes with the sign of the hydrostatic stress, σ_{kk}. Figure 8 shows the response of the improved model and the Goldberg model to a hydrostatic stress state, which was achieved by applying uniform strain-controlled compression at a strain rate of 1,000/s in each of the normal directions at 25 °C. Note that the compressive plastic Poisson's ratio for E862, determined via calibration against experimental data, is 0.5, which implies the material is plastically incompressible in compression. For solely the simulation results presented in Figure 8, the tensile and compressive plastic Poisson's ratios have been set to 0.3 and 0.4, respectively ($\gamma = 4.23\times10^{-3};\ \xi = 23.79\times10^{-3}$) so that the model can simulate nonisochoric plastic deformation under hydrostatic compression. Additionally, since the Goldberg model is technically not defined for hydrostatic loading (due to division by $J_2 = 0$), the third line of Equation (9) was used to compute the inelastic strain rate tensor components, where A is set equal to A_{UT}, which in this case is 0.088. All other model parameters in the Goldberg model and the improved model are unchanged. In Figure 8(a), the Goldberg model pressure versus volumetric strain curve becomes nearly vertical at a volumetric strain of approximately –0.1. In Figure 8(b), the plastic volumetric strain has the wrong sign because the deviatoric stresses are zero and the hydrostatic state variable in the Goldberg model does not change signs with pressure. In the improved model, the elastic and plastic volumetric strains are both negative, as they should be under hydrostatic compression. Figure 8(c) shows the effective stress and the accumulated plastic work density as a function of the accumulated effective inelastic strain. The Goldberg model predicts a negative effective stress because the hydrostatic state variable does not change signs with pressure. Since the effective inelastic strain is always positive, the plastic work density is negative, which is thermodynamically incorrect. The improved model predicts positive plastic work density because the effective stress has been constrained to always be nonnegative.

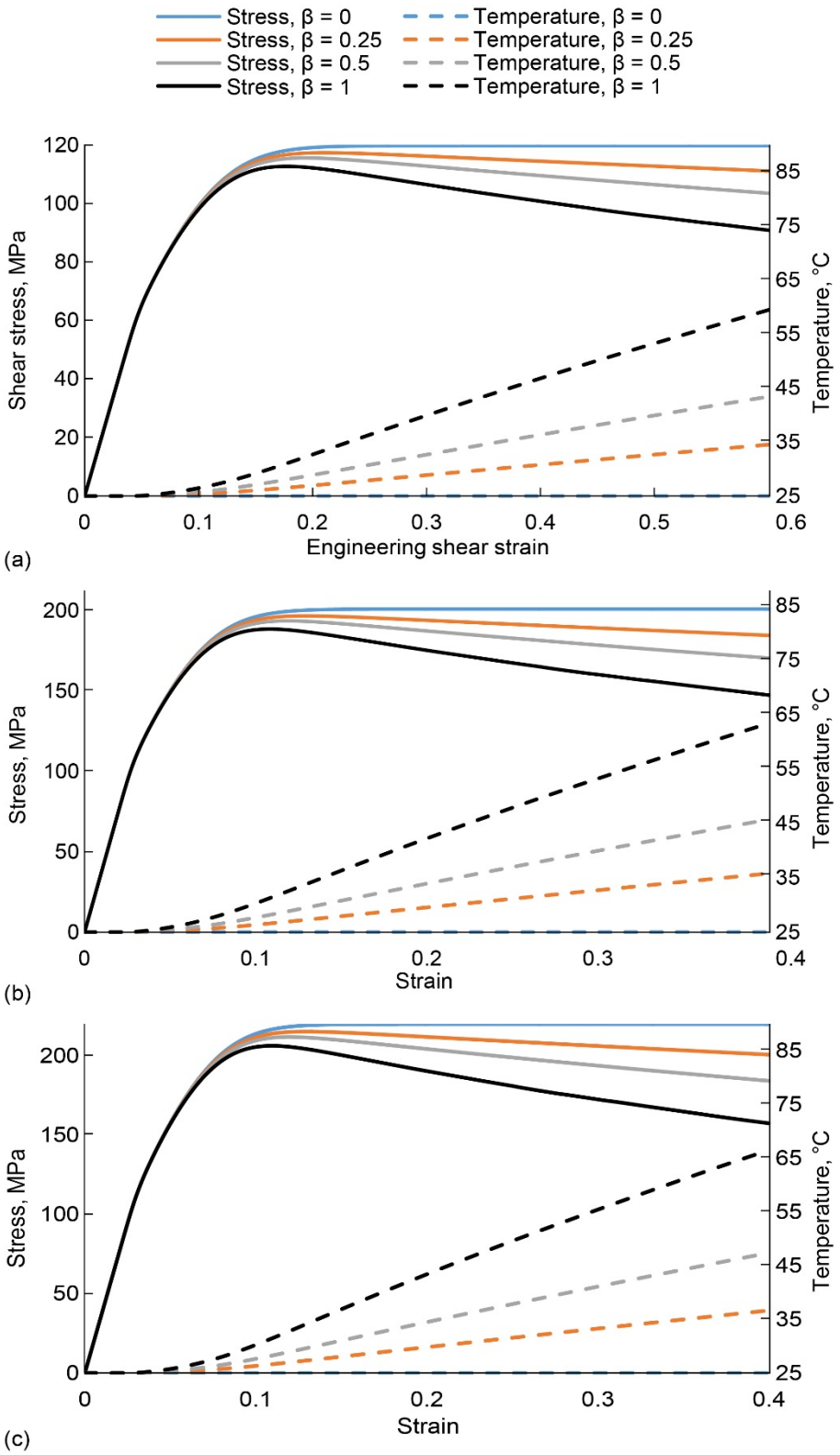

Figure 6.—Effect of varying inelastic heat fraction on (a) shear, (b) tensile, and (c) compressive stress-strain and temperature-strain response.

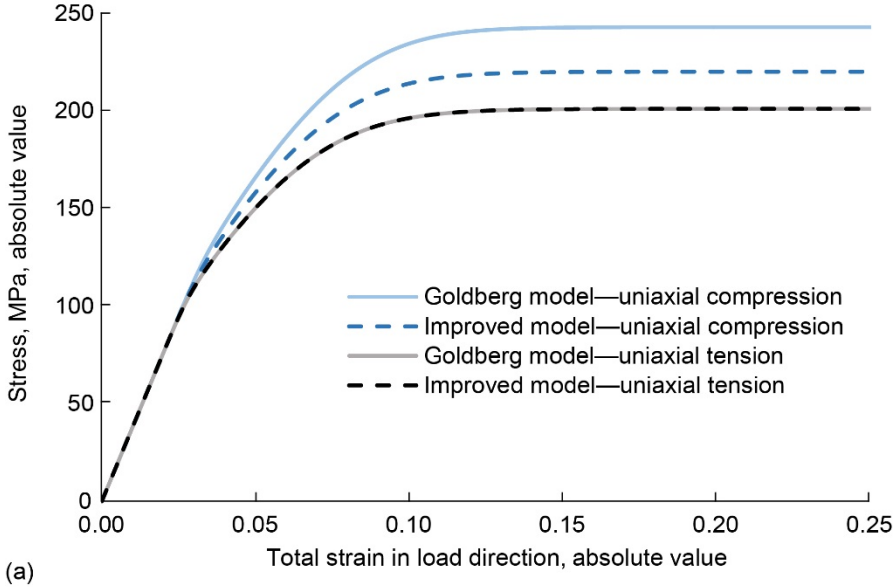

(a)

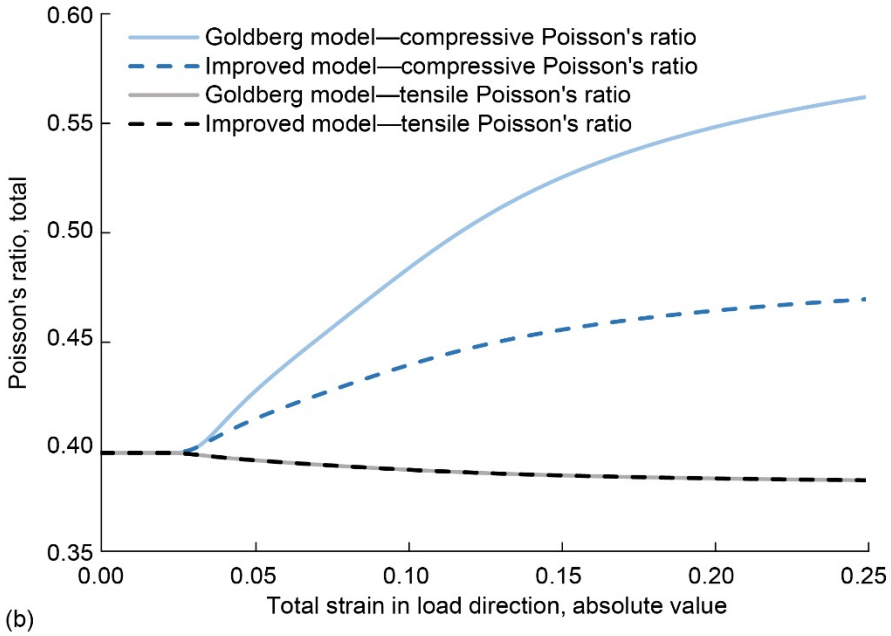

(b)

Figure 7.—(a) Stress and (b) Poisson's ratio as a function of strain in the load direction for simulated uniaxial tensile and compressive loading.

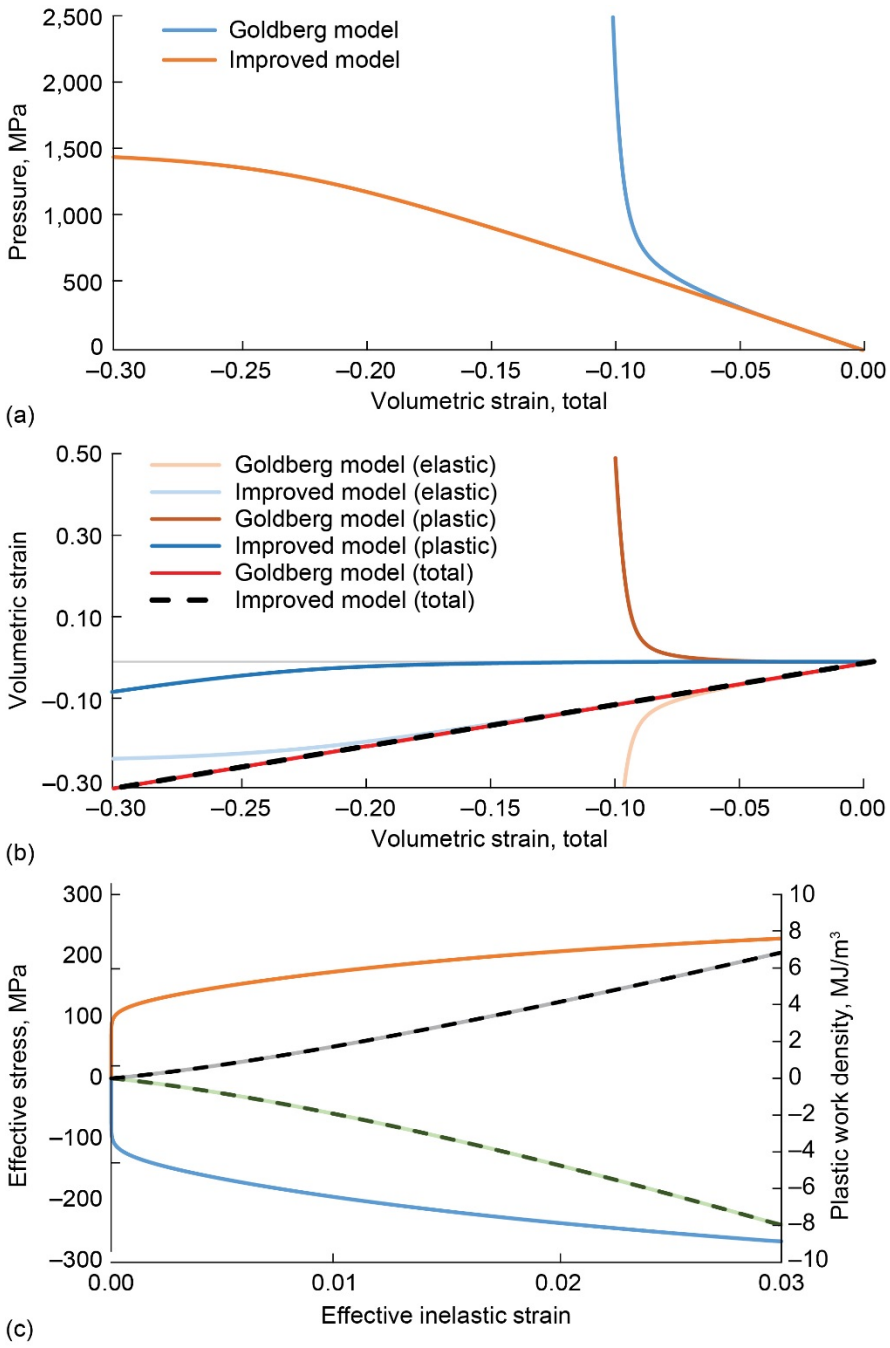

Figure 8.—Response of Goldberg model and improved model to hydrostatic stress state: (a) Pressure vs. volumetric strain; (b) Elastic, plastic and total volumetric strain components vs. total volumetric strain.

4.2 Response of Unidirectional Composite

The effects of adiabatic heating on the uniaxial tension, uniaxial compression and in-plane shear response of a unidirectional composite are investigated in this section. As in previous research (Sorini et al. 2019), a linear elastic response with no significant adiabatic heating or thermal softening is observed for longitudinal loading. As such, simulation results are only presented for transverse tensile, transverse compressive, and in-plane shear loading. Simulation results are presented for a T700/E862 unidirectional composite with a 60 percent fiber volume fraction at strain rates of 100 and 1,000/s. The T700 fiber properties used in the simulations are presented in Table III (Cater et al. 2015); the fibers have been modeled as transversely isotropic and linear elastic and their material properties are assumed to not vary with temperature. The properties used for the matrix subcells are given in Table II. It should be noted that, currently, there is no unidirectional T700/E862 composite test data available; this material system was selected due to the availability of fiber and matrix material properties and experimental data (for E862). To examine qualitatively the effects of adiabatic heating, simulations are conducted with inelastic heat fractions of zero (isothermal) and unity. An inelastic heat fraction of unity corresponds to a case where all plastic work is converted to heat. This implies that the simulated temperature rises in this section represent an upper bound, though Garg et al. (2008) found experimentally that nearly all the inelastic work was converted to heat in the high rate uniaxial compression of polycarbonate, implying that assuming an inelastic heat fraction of unity may be fairly accurate for adiabatic conditions. It should be noted that damage and failure are not included in the simulations in this section; all nonlinearity is due to inelasticity.

The response of the unidirectional composite subjected to transverse tensile loading at strain rates of 100 and 1,000/s at room temperature is shown in Figure 9(a) and (b), respectively. The transverse compressive response at the same strain rates is shown in Figure 10(a) and (b). Since the transverse response of a unidirectional composite is matrix dominated, significant adiabatic heating and thermal softening are observed for both transverse tensile and compressive loading. The RUC average temperature rises for the 100 and 1,000/s strain rate transverse tension simulations were 21.60 and 25.12 °C, respectively, whereas the maximum local (subcell level) temperature rises were 94.92 and 110.33 °C. The RUC average temperature rises for the 100 and 1,000/s strain rate transverse compression simulations were 27.12 and 31.20 °C, respectively, whereas the maximum local (subcell level) temperature rises were 117.36 and 132.48 °C. It is evident that, for the same strain rate and level of total deformation, the transverse compression simulations displayed larger temperature rises than the transverse tension simulations. It is evident from Figure 9 and Figure 10 that the tension-compression asymmetry in the composite response is captured in the simulations; the magnitude of the transverse compressive saturation stress is larger than the transverse tensile saturation stress.

Figure 11(a) and (b) show the response of the unidirectional composite subjected to in-plane shear loading at room temperature at engineering shear strain rates of 100 and 1,000/s, respectively. Significant thermal softening due to adiabatic heating in the matrix is observed. The RUC average temperature rises for the 100 and 1,000/s engineering shear strain rate simulations were 9.79 and 11.51 °C, respectively. The maximum local (subcell level) temperature rises were 48.37 and 58.75 °C.

TABLE III.—T700 CARBON FIBER ELASTIC PROPERTIES

Axial Young's Modulus	230 GPa
Transverse Young's Modulus	15 GPa
Axial Poisson's Ratio	0.2
Transverse Poisson's Ratio	0.3
In-Plane Shear Modulus	27 GPa

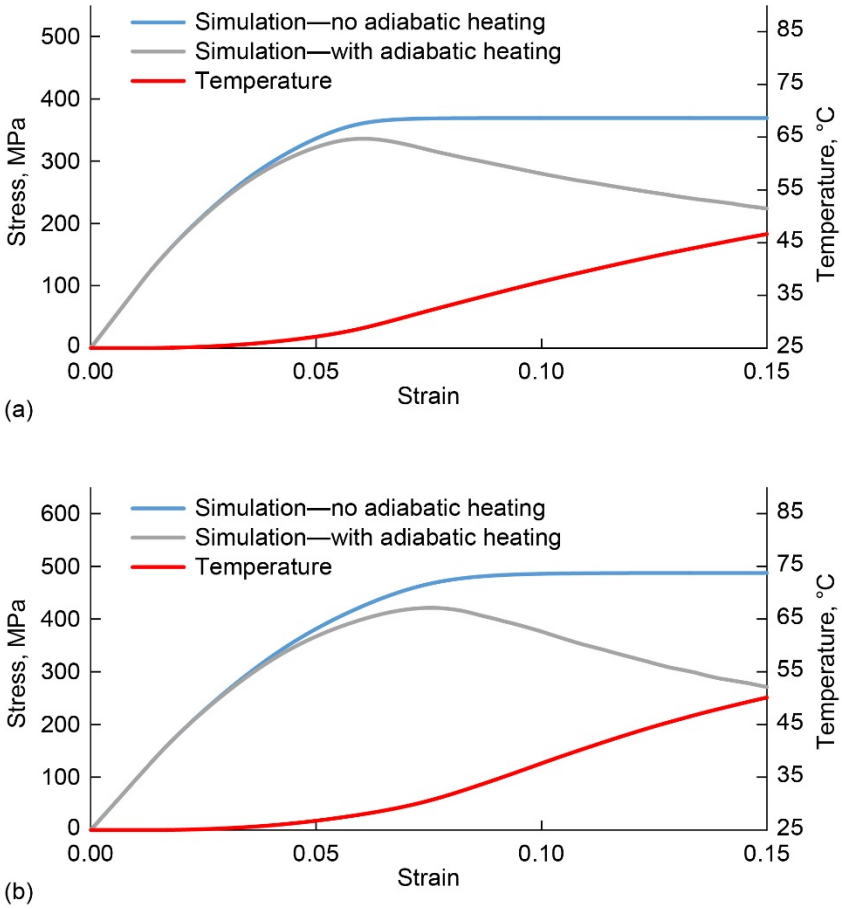

Figure 9.—Simulated transverse tensile response of unidirectional composite at strain rates of (a) 100/s and (b) 1,000/s.

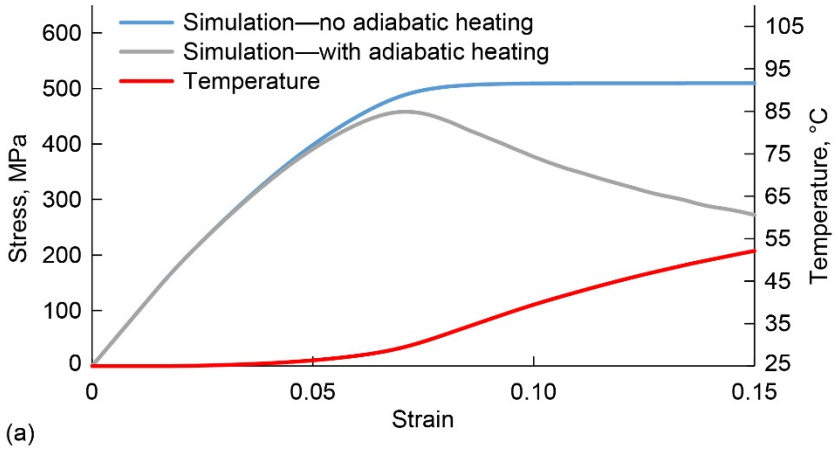

(a)

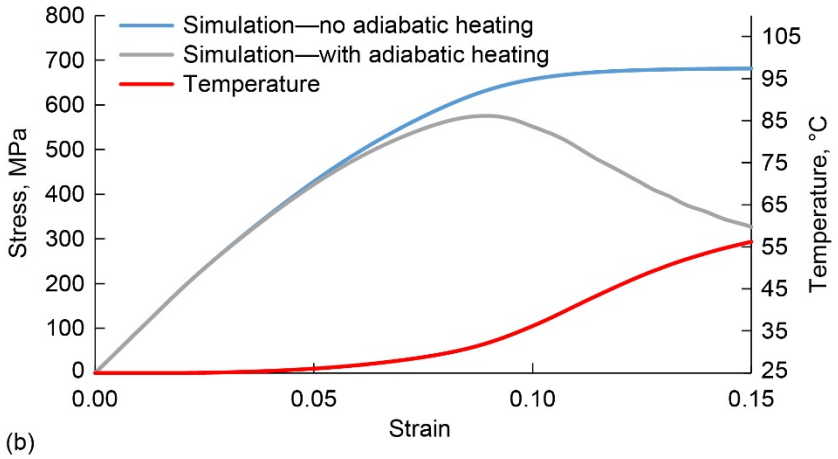

(b)

Figure 10.—Simulated transverse compressive response of unidirectional composite at strain rates of (a) 100/s and (b) 1,000/s.

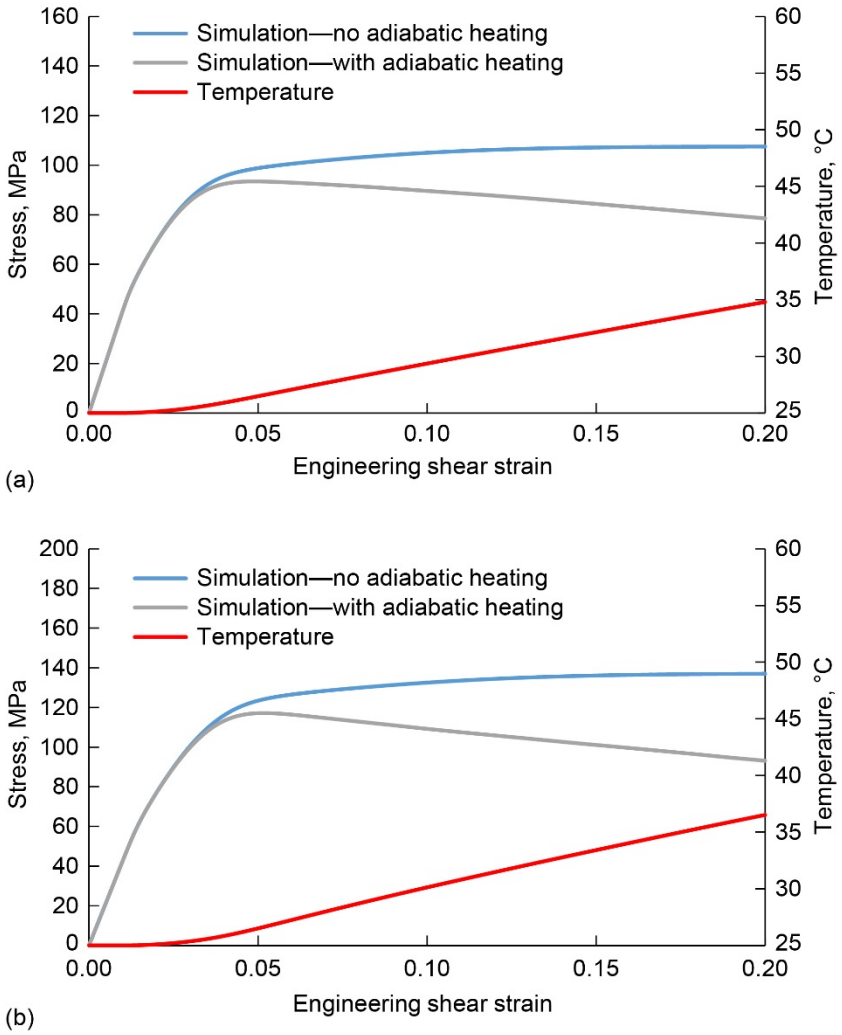

Figure 11.—Simulated in-plane shear response of unidirectional composite at strain rates of (a) 100/s and (b) 1,000/s.

5.0 Concluding Remarks

A plastically dilatant unified viscoplastic constitutive formulation suitable for use in multiscale composite impact problems has been presented. A new plastic potential function was proposed, where two hydrostatic constants control the level of influence of hydrostatic stresses on plastic deformation. Elementary loading conditions were used to obtain relations between model constants to ensure physically realistic plastic flow and a nonnegative effective stress, which subsequently guarantees nonnegative plastic dissipation, a necessary thermodynamic requirement. Relations between the tensile and compressive plastic Poisson's ratios and the two hydrostatic constants were derived and a procedure to determine their values, as well as the other model constants, was presented. The model is strain rate, temperature, and pressure dependent and was shown to be capable of representing test data of a representative epoxy over a range of strain rates, temperatures, and loading conditions (shear, tension, and compression). The two hydrostatic constants used in the model permit the user to independently vary the tensile and compressive Poisson's ratios, which would not be possible using a single hydrostatic constant. Adiabatic temperature rises are predicted using the heat energy equation, neglecting the thermoelastic and conduction terms. The unified viscoplastic model was used as a constitutive model in the GMC micromechanics framework, including the adiabatic heat energy equation, to illustrate the effects of adiabatic heating on the response of a T700/E862 unidirectional composite. Significant thermal softening due to adiabatic heating was observed for transverse tensile, transverse compressive, and in-plane shear loading, highlighting the importance of including the effects of adiabatic heating in multiscale analyses of PMCs under dynamic loading, where the composite is in a complex multiaxial stress state. The semi-analytical micromechanics model is suitable for implementation into a commercial finite element code as a user defined material subroutine, which is the subject of future work. It is anticipated that the improved constitutive formulation, as well as including the effects of adiabatic heating and subsequent thermal softening, will improve model predictions of the impact response of PMC structures.

Appendix—Comparison of Epon 862 Uniaxial Tensile and Compressive True Stress-Strain Curves Computed Using Equations (36) and (37)

A comparison of the E862 uniaxial tensile and compressive true stress-strain curves computed using Equations (36) and (37) is shown in Figure 12 and Figure 13. The data used for the conversions from engineering to true stress-strain can be found in Littell (2008) and Littell et al. (2008). In Figure 12 and Figure 13, the dashed curves were computed using Equation (36) and the solid (corrected) curves were computed using Equation (37).

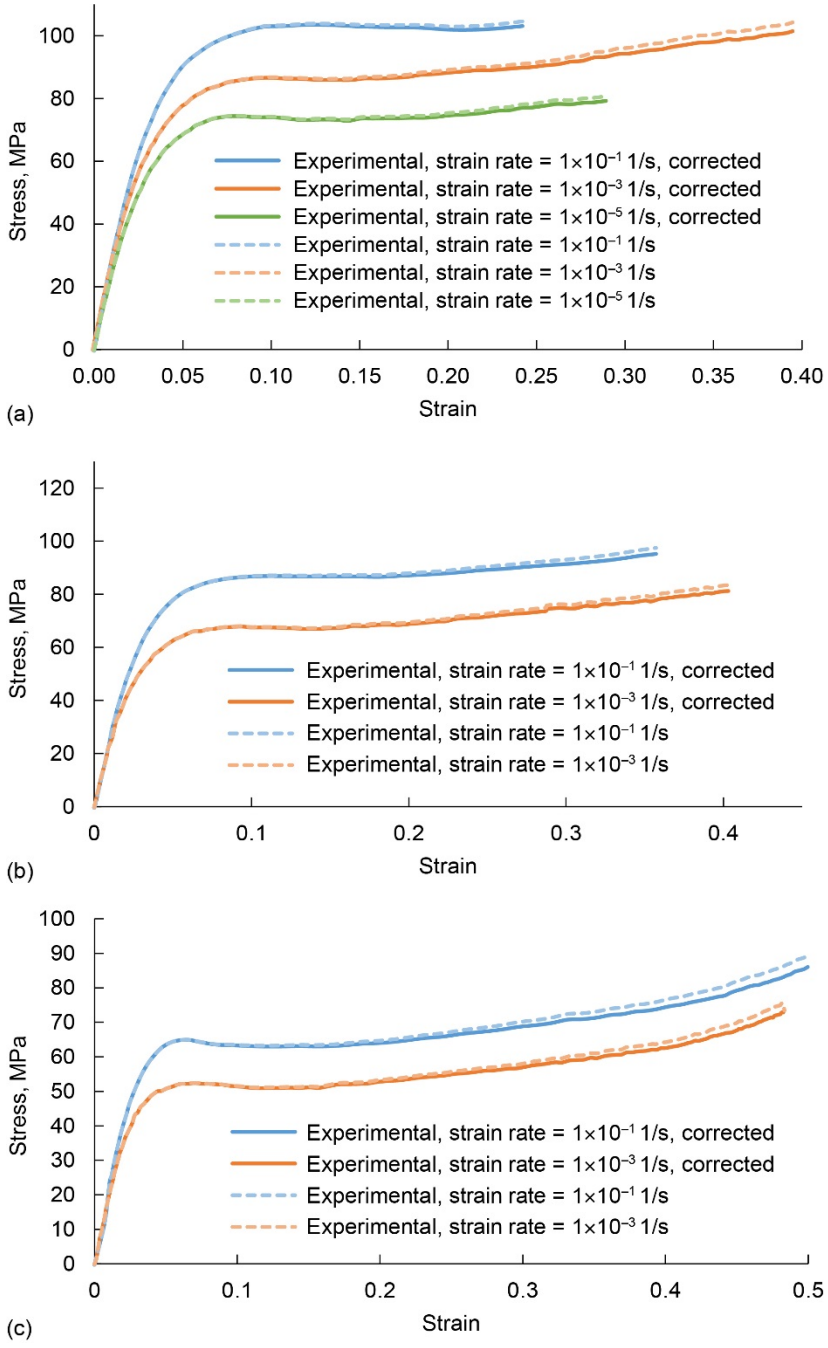

Figure 12.—Comparison of experimental tensile true stress-strain response of Epon 862 epoxy determined using Equations (36) and (37) at (a) Room temperature (25 °C); (b) 50 °C; (c) 80 °C.

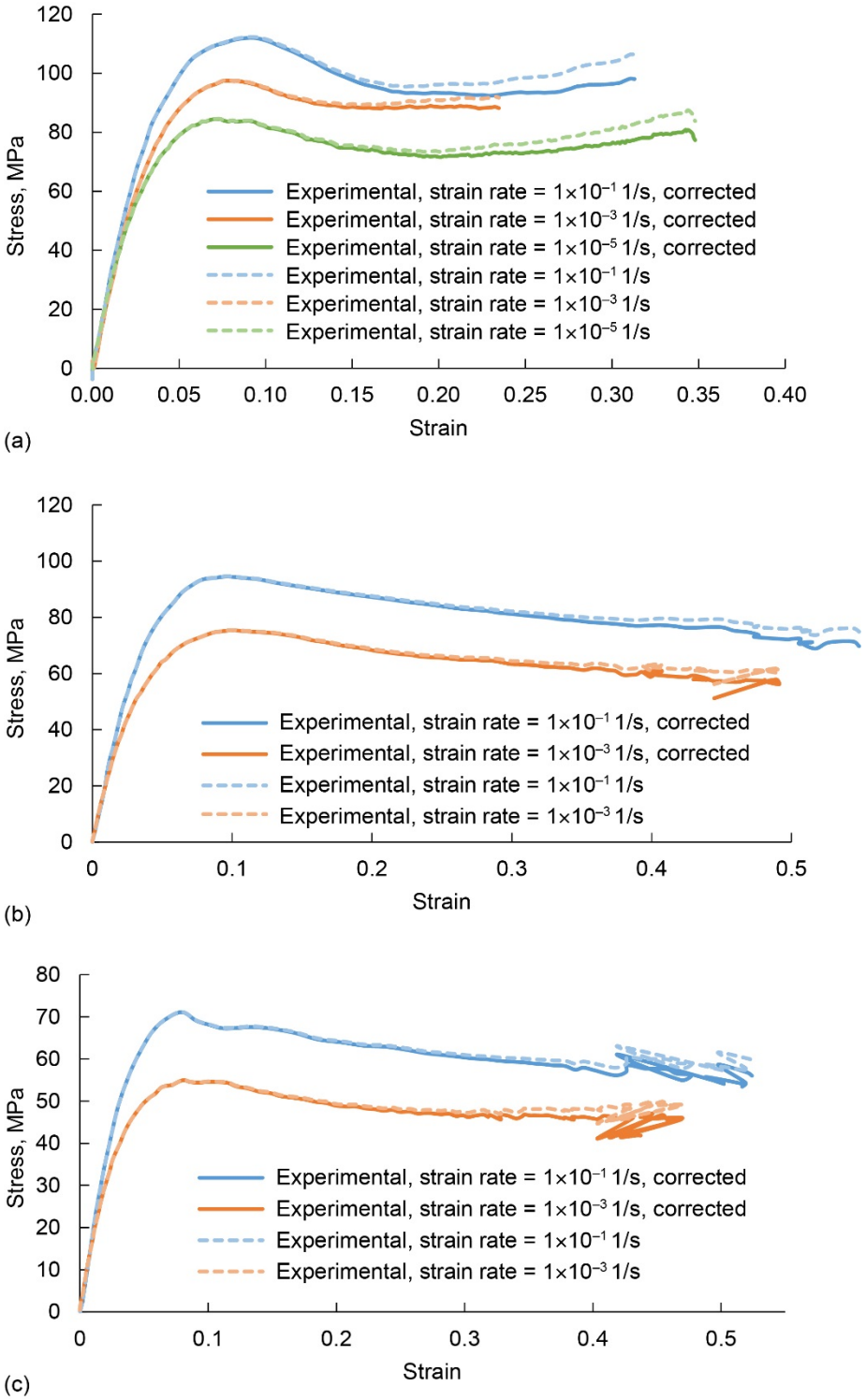

Figure 13.—Comparison of experimental compressive true stress-strain response of Epon 862 epoxy determined using Equations (36) and (37) at (a) Room temperature (25 °C); (b) 50 °C; (c) 80 °C.

References

Aboudi, J., Arnold, S. M., & Bednarcyk, B. A. (2012). *Micromechanics of composite materials: a generalized multiscale analysis approach*. Butterworth-Heinemann.

Arnold, S. M., Lerch, B., & Ricks, T. M. (2019). Interpretation of Experimental Tensile Test Results and Its Implication on Damage Modeling. In *AIAA Scitech 2019 Forum* (p. 1965).

Arruda, E. M., Boyce, M. C., & Jayachandran, R. (1995). Effects of strain rate, temperature and thermomechanical coupling on the finite strain deformation of glassy polymers. *Mechanics of Materials*, *19*(2-3), 193-212.

Bednarcyk, B. A., Aboudi, J., Arnold, S. M., & Pineda, E. J. (2019). A multiscale two-way thermomechanically coupled micromechanics analysis of the impact response of thermo-elastic-viscoplastic composites. *International Journal of Solids and Structures*, *161*, 228-242.

Bhattachar, V. S., & Stouffer, D. C. (1993). Constitutive Equations for the Thermomechanical Response of René 80: Part 1—Development From Isothermal Data. *Journal of Engineering Materials and Technology*, *115*(4), 351-357.

Bhattachar, V. S. (1991). A unified constitutive model for the thermomechanical fatigue response of a nickel base superalloy Rene 80. Dissertation. University of Cincinnati.

Bodner, S. R. (2001). Unified plasticity for engineering applications. (Vol. 47). Springer Science & Business Media.

Bodner, S., & Partom, Y. (1975). Constitutive equations for elastic-viscoplastic strain-hardening materials. *Journal of Applied Mechanics*, *42*(2), 385-389.

Cater, C., Xiao, X., Goldberg, R. K., & Kohlman, L. W. (2015). Experimental and Numerical Analysis of Triaxially Braided Composites Utilizing a Modified Subcell Modeling Approach. NASA/TM—2015-218814, National Aeronautics and Space Administration, Washington, DC.

Chen, J. K., Allahdadi, F. A., & Sun, C. T. (1997). A quadratic yield function for fiber-reinforced composites. *Journal of Composite Materials*, *31*(8), 788-811.

Chen, J. L., & Sun, C. T. (1993). A plastic potential function suitable for anisotropic fiber composites. *Journal of Composite Materials*, *27*(14), 1379-1390.

Chiou, S. T., Tsai, H. L., & Lee, W. S. (2007). Effects of strain rate and temperature on the deformation and fracture behaviour of titanium alloy. Materials transactions, 48(9), 2525-2533.

Chou, S. C., Robertson, K. D., & Rainey, J. H. (1973). The effect of strain rate and heat developed during deformation on the stress-strain curve of plastics. *Experimental Mechanics*, *13*(10), 422-432.

Chow, C. L., & Lu, T. J. (1989). On evolution laws of anisotropic damage. *Engineering Fracture Mechanics*, *34*(3), 679-701.

Faria, R., Oliver, J., & Cervera, M. (1998). A strain-based plastic viscous-damage model for massive concrete structures. *International Journal of Solids and Structures*, *35*(14), 1533-1558.

Garg, M., Mulliken, A. D., & Boyce, M. C. (2008). Temperature rise in polymeric materials during high rate deformation. *Journal of Applied Mechanics*, *75*(1), 011009.

Gilat, A., Goldberg, R. K., & Roberts, G. D. (2007). Strain rate sensitivity of epoxy resin in tensile and shear loading. *Journal of Aerospace Engineering*, *20*(2), 75-89.

Goldberg, R. K., Roberts, G. D., & Gilat, A. (2005). Implementation of an associative flow rule including hydrostatic stress effects into the high strain rate deformation analysis of polymer matrix composites. *Journal of Aerospace Engineering*, *18*(1), 18-27.

Johnston, J. P., Pereira, J. M., Ruggeri, C. R., & Roberts, G. D. (2018). High-speed infrared thermal imaging during ballistic impact of triaxially braided composites. *Journal of Composite Materials*, *52*(25), 3549-3562.

Jordan, J. L., Foley, J. R., & Siviour, C. R. (2008). Mechanical properties of Epon 826/DEA epoxy. *Mechanics of Time-Dependent Materials*, *12*(3), 249-272.

Kawai, M., Zhang, J. Q., Xiao, Y., & Hatta, H. (2010). Modeling of tension-compression asymmetry in off-axis nonlinear rate-dependent behavior of unidirectional carbon/epoxy composites. *Journal of Composite Materials*, *44*(1), 75-94.

Kenaga, D., Doyle, J. F., & Sun, C. T. (1987). The characterization of boron/aluminum composite in the nonlinear range as an orthotropic elastic-plastic material. *Journal of Composite Materials*, *21*(6), 516-531.

Kendall, M. J., & Siviour, C. R. (2013). Experimentally simulating adiabatic conditions: approximating high rate polymer behavior using low rate experiments with temperature profiles. *Polymer*, *54*(18), 5058-5063.

Kolling, S., Haufe, A., Feucht, M., & Du Bois, P. A. (2005). SAMP-1: A Semi-Analytical Model for the Simulation of Polymers. In: 4th German LS-DYNA Forum (LS-DYNA Anwenderforum), Bamberg, Germany, 20-21 October 2005.

Li, Z., & Lambros, J. (2001). Strain rate effects on the thermomechanical behavior of polymers. *International Journal of Solids and Structures*, *38*(20), 3549-3562.

Littell, J. (2008). The experimental and analytical characterization of the macromechanical response for triaxial braided composite materials. (Doctoral dissertation, University of Akron).

Littell, J. D., Ruggeri, C. R., Goldberg, R. K., Roberts, G. D., Arnold, W. A., & Binienda, W. K. (2008). Measurement of epoxy resin tension, compression, and shear stress–strain curves over a wide range of strain rates using small test specimens. *Journal of Aerospace Engineering*, *21*(3), 162-173.

Lubliner, J. (2008). *Plasticity Theory*. Courier Corporation.

Mulliken, A. D., & Boyce, M. C. (2006). Mechanics of the rate-dependent elastic–plastic deformation of glassy polymers from low to high strain rates. *International Journal of Solids and Structures*, *43*(5), 1331-1356.

Paley, M., & Aboudi, J. (1992). Micromechanical analysis of composites by the generalized cells model. *Mechanics of Materials*, *14*(2), 127-139.

Pan, Z., Sun, B., Shim, V. P., & Gu, B. (2016). Transient heat generation and thermo-mechanical response of epoxy resin under adiabatic impact compressions. *International Journal of Heat and Mass Transfer*, *95*, 874-889.

Pindera, M. J., & Bednarcyk, B. A. (1999). An efficient implementation of the generalized method of cells for unidirectional, multi-phased composites with complex microstructures. *Composites Part B: Engineering*, *30*(1), 87-105.

Poulain, X. (2010). On the thermomechanical behavior of epoxy polymers: Experiments and modeling. (Doctoral dissertation, Ph. D. thesis, Texas A & M University, College Station, TX).

Poulain, X., Benzerga, A. A., & Goldberg, R. K. (2014). Finite-strain elasto-viscoplastic behavior of an epoxy resin: Experiments and modeling in the glassy regime. *International Journal of Plasticity*, *62*, 138-161.

Poulain, X., Kohlman, L. W., Binienda, W., Roberts, G. D., Goldberg, R. K., & Benzerga, A. A. (2013). Determination of the intrinsic behavior of polymers using digital image correlation combined with video-monitored testing. *International Journal of Solids and Structures*, *50*(11-12), 1869-1878.

Richeton, J., Ahzi, S., Vecchio, K. S., Jiang, F. C., & Makradi, A. (2007). Modeling and validation of the large deformation inelastic response of amorphous polymers over a wide range of temperatures and strain rates. *International Journal of Solids and Structures*, *44*(24), 7938-7954.

Rittel, D. (1999). On the conversion of plastic work to heat during high strain rate deformation of glassy polymers. *Mechanics of Materials*, *31*(2), 131-139.

Robinson, D. N., & Binienda, W. K. (2001). Model of viscoplasticity for transversely isotropic inelastically compressible solids. *Journal of Engineering Mechanics*, *127*(6), 567-573.

Robinson, D. N., Tao, Q. and Verrilli, M. J. (1994). A hydrostatic stress-dependent anisotropic model of viscoplasticity. NASA TM 106525, National Aeronautics and Space Administration, Washington, DC.

Rowghanian P., Hoa S.V. (2011). Improvement of Temperature Distribution Across Thick Thermoset Composite Laminates Using Carbon Nanotubes. In: American Society for Composites 26th Technical Conference Proceedings (ASC/26), Montreal, Quebec, Canada, 26-28 September 2011. p. 188-201.

Siviour, C. R., & Jordan, J. L. (2016). High strain rate mechanics of polymers: a review. *Journal of Dynamic Behavior of Materials*, *2*(1), 15-32.

Sorini, C., Chattopadhyay, A., & Goldberg, R. K. (2019). Micromechanical modeling of the effects of adiabatic heating on the high strain rate deformation of polymer matrix composites. *Composite Structures*, 215, 377-384.

Spurgeon, W. A. (2018). Thermal Conductivities of Some Polymers and Composites (No. ARL-TR-8298). US Army Research Laboratory Aberdeen Proving Ground United States.

Sun, C. T., & Chen, J. L. (1989). A simple flow rule for characterizing nonlinear behavior of fiber composites. *Journal of Composite Materials*, *23*(10), 1009-1020.

Thiruppukuzhi, S. V., & Sun, C. T. (1998). Testing and modeling high strain rate behavior of polymeric composites. *Composites Part B: Engineering*, *29*(5), 535-546.

Trojanowski, A., Ruiz, C., & Harding, J. (1997). Thermomechanical properties of polymers at high rates of strain. *Le Journal de Physique IV*, *7*(C3), C3-447.

Varghese, A. G., and R. C. Batra. "Constitutive equations for thermomechanical deformations of glassy polymers." *International Journal of Solids and Structures* 46.22 (2009): 4079-4094.

Walley, S. M., Field, J. E., Pope, P. H., & Safford, N. A. (1989). A study of the rapid deformation behaviour of a range of polymers. *Philosophical Transactions of the Royal Society of London. Series A*, *Mathematical and Physical Sciences*, *328*(1597), 1-33.

Wang, J., & Xiao, Y. (2017a). Some improvements on Sun–Chen's one-parameter plasticity model for fibrous composites–part I: constitutive modelling for tension–compression asymmetry response. *Journal of Composite Materials*, *51*(3), 405-418.

Wang, J., & Xiao, Y. (2017b). Some improvements on Sun-Chen's one-parameter plasticity model for fibrous composites (Part II: Finite element method implementation and applications). *Journal of Composite Materials*, *51*(4), 533-545.

Weeks, C. A., & Sun, C. T. (1998). Modeling non-linear rate-dependent behavior in fiber-reinforced composites. *Composites Science and Technology*, *58*(3-4), 603-611.

Yokozeki, T., Ogihara, S., Yoshida, S., & Ogasawara, T. (2007). Simple constitutive model for nonlinear response of fiber-reinforced composites with loading-directional dependence. *Composites Science and Technology*, *67*(1), 111-118.